

V. AnSb. Actinide monoantimonides

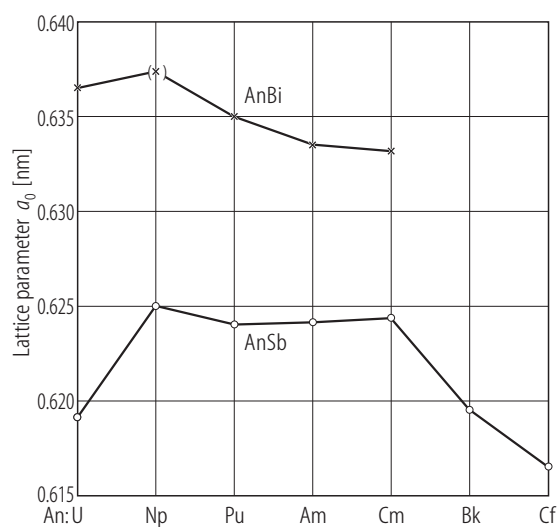


Fig. V.1. AnSb, AnBi. Lattice parameters, a_0 , vs. actinide element from U to Cf (AnSb) and from U to Cm (AnBi) [87GH]. The small difference obtained between parameters a_0 of AmBi or CmBi compared to those reported in [74R] and [75CBDM], respectively, is caused by difference in radiation damages.

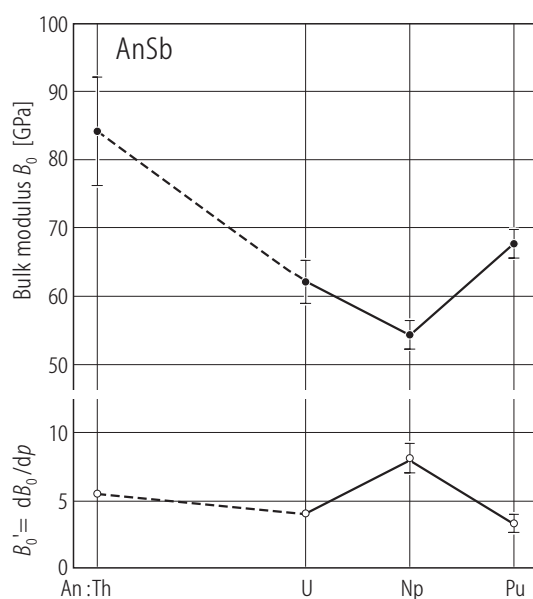


Fig. V.2. AnSb. Bulk moduli, B_0 (lhs), and pressure derivatives, B'_0 (rhs), for the actinide monoantimonides series as a function of the atomic number Z of the actinide element [90DB]. See the tendency to decreasing bulk moduli to its minimum for NpSb. For the values see Table 6.

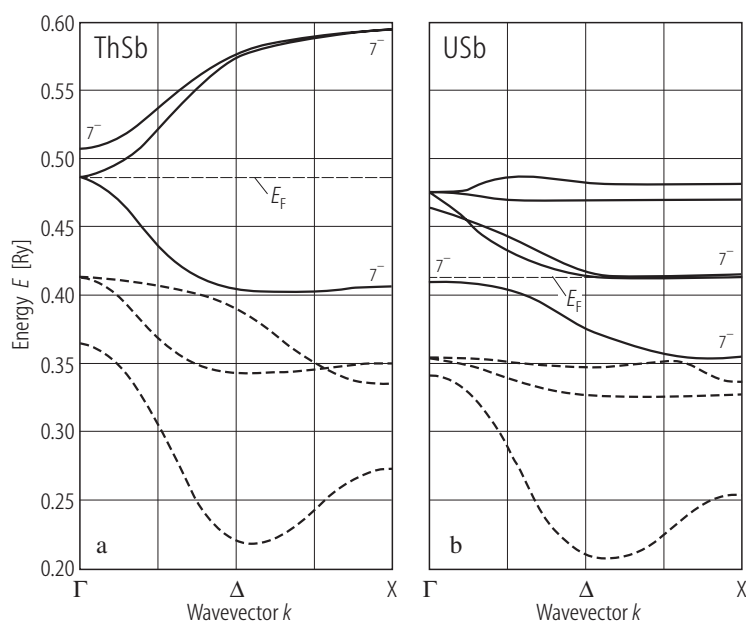


Fig. V.3. ThSb, USb. Energy band structures of (a) ThSb and (b) USb along the Γ X symmetry line in the vicinity of their Fermi energy [80WP]. The valence p-bands are shown as dashed lines. The fully relativistic (KKR) method with CPA is applied in calculations. Note that the main changes in the top VB region, when going from Th- to U-antimonide, are caused by the f-electrons.

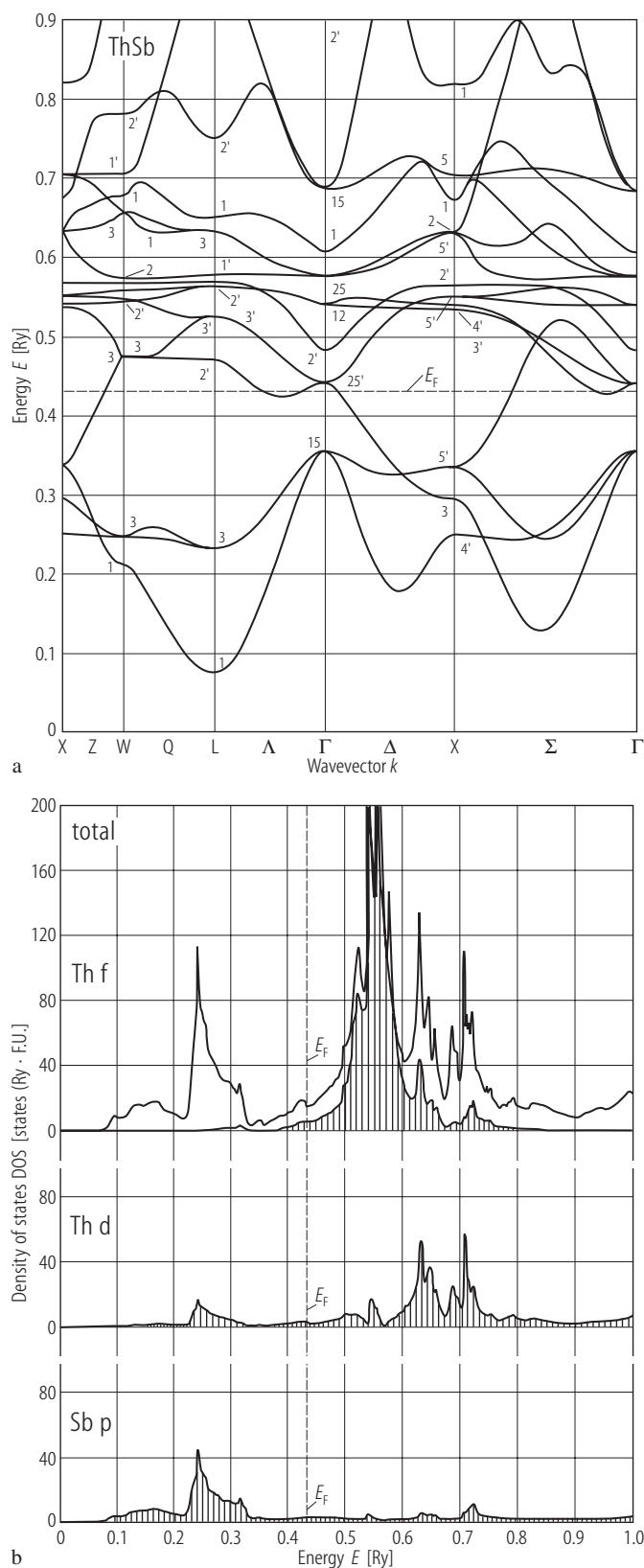
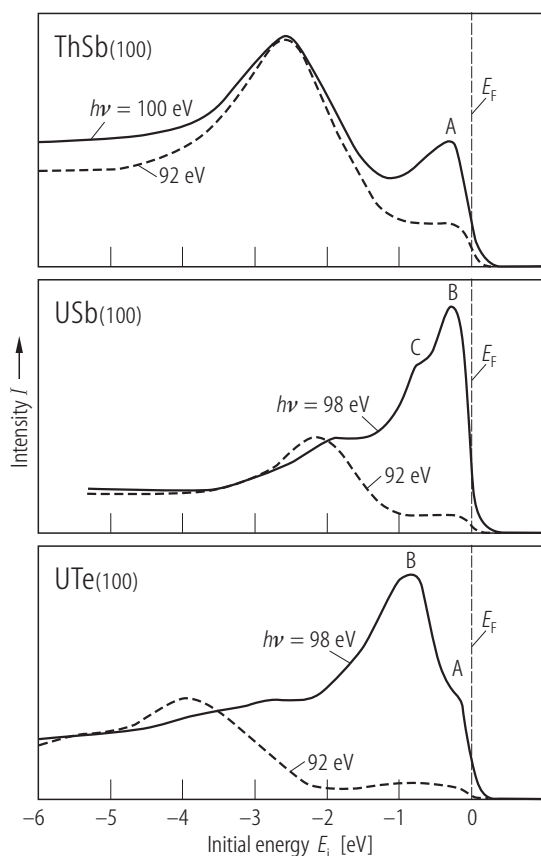


Fig. V.4. ThSb. **(a)** Self-consistent APW band structure with the LDA along symmetry axes in the BZ [90TK1]. No large difference is observed to the band structure of LaSb. The lowest three bands are dominated by the Sb 5p states, the upper Th 6d and 5f states mix appreciably. **(b)** Total and partial DOS [90TK1]. The narrow bands at about 0.55 Ry are derived primarily from the Th 5f states. At the Γ point, the dominant Th 5f states are those labeled by 2', 25 and 15, while the dominant Th 6d states are 25' and 12 ones. For detailed description of NaCl-type band structures see [80H].



←

Fig. V.5. ThSb, USb, s.c. Normalized EDC's of ThSb and USb compared to UTe taken at resonance (≈ 100 eV) and off-resonance (92 eV) [82RMEA]. One notes a marked difference between the thorium and the uranium compounds. From the 92 eV spectra (5f emission is minimum) was established the location of the p-band peaks at 2.1 eV for USb and 3.9 eV for UTe.

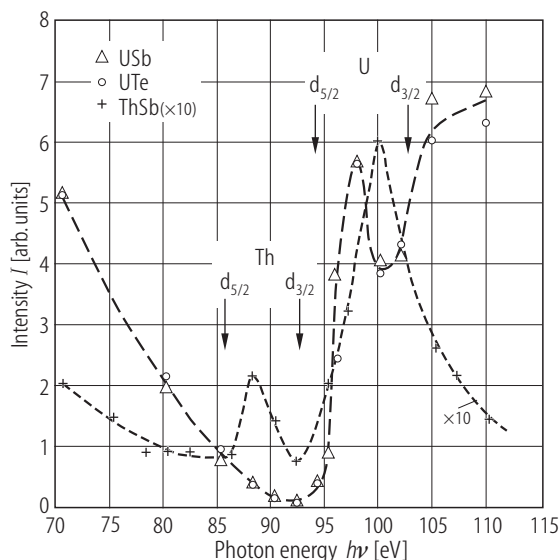
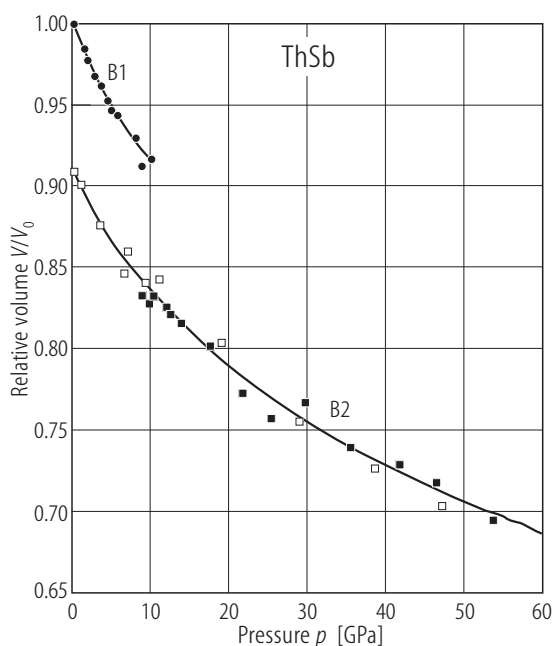


Fig. V.6. ThSb, USb, s.c. The constant initial state (CIS) spectra obtained from EDC's for ThSb and USb in the CB regions and compared to those in UTe [82RMEA]. The arrows show the Th and U 5d core absorption edges from [74FBWF]. These results are in good qualitative agreement with the results of USb by [80BBBP] shown in Fig. V.25. Note that normalized at $h\nu = 98$ eV intensity variations for USb (open triangles) and UTe (open circles) fall on a common curve which indicates that USb and UTe have the same $5f^3$ configuration. On the other hand, the shape of the CIS curve of ThSb is quite different to that of USb and UTe due to the difference in Fano resonance edges of the 5d ionization energies. It appears however that at $h\nu = 92$ eV both the Th and U emission is at a minimum.



←

Fig. V.7. ThSb. Relative volume, V/V_0 , vs. pressure, p , at RT [88GSBD]. $a_0(\text{B1}) = 0.6318(1)$ nm. At 10 GPa a B1 – B2 transition takes place with a volume collapse of 9.1 %. The solid lines are the fittings to the equations of state. Note that a large hysteresis exists down to zero pressure. $a_0(\text{B2}) = 0.3247(5)$ nm.

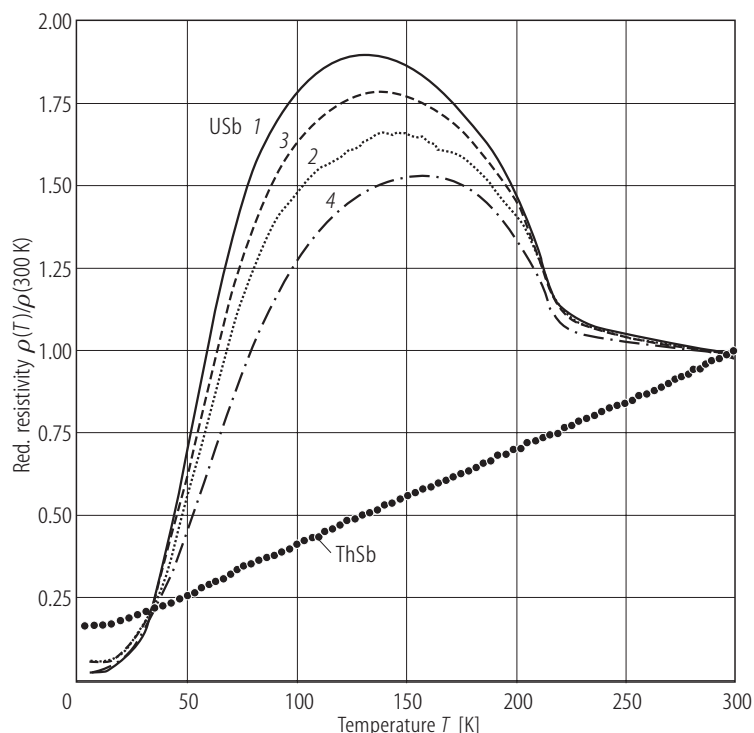


Fig. V.8. ThSb, USb s.c. Reduced electrical resistivity, $\rho(T)/\rho(300\text{ K})$, vs. T for USb ($a = 0.621\text{ nm}$) with different RRR: Curve 1 – 18.6, 2 – 38.6, 3 – 15.9 and 4 – 35.7 and compared with that of ThSb [95OHHS]. The absolute values of the resistivity of USb and ThSb at 300 K are about 600 and 50 $\mu\Omega\text{cm}$, respectively.

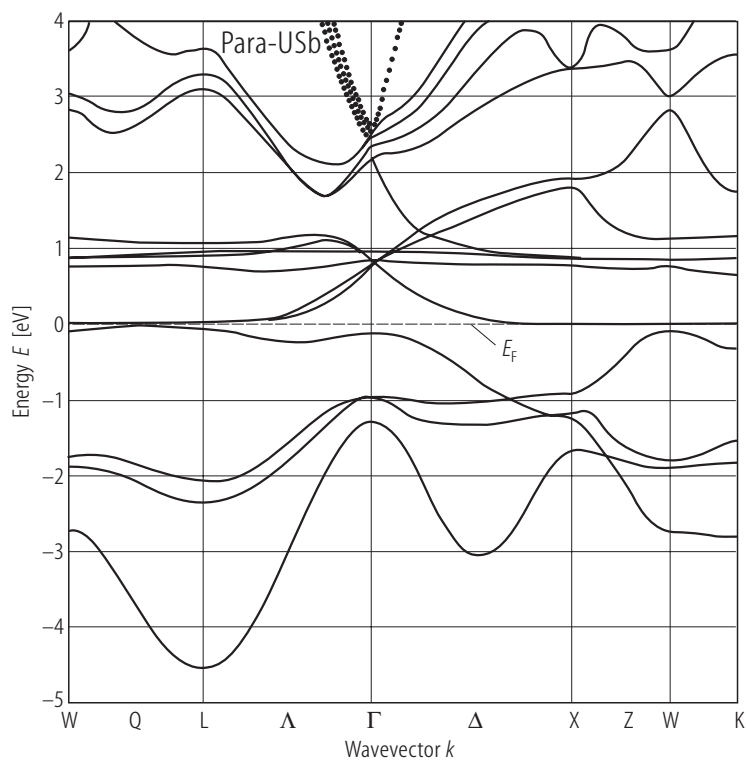


Fig. V.9. USb. Electronic band structure determined by RSP-LAPW method in the paramagnetic state [00Y]. This structure is in agreement with the fully relativistic KKR calculation (see [80WP]). Note at the bottom the Sb 5p states (the U 6p and Sb 5s valence bands are omitted) being mixed strongly with the U-d component. The narrow bands in the energy range from 0.4 to 0.5 Ry are from U 5f states which are split into two sub-bands with $\gamma = 5/2$ and $7/2$ states. In the same energy region, the dispersive parts around the Γ point are the U 5f states hybridized with the U 6d states. At higher energies there are unoccupied U 6d broaden bands. The electron distribution at the U site is 1.3d+2.8f, while at the Sb site is 1.4s+2.0p. Calculated DOS at E_F gives $\gamma_b = 63.74\text{ mJ/K}^2\text{mol}$ which is much larger compared to the experimental value $\gamma(0) = 4.56\text{ mJ/K}^2\text{mol}$ [84SFV].

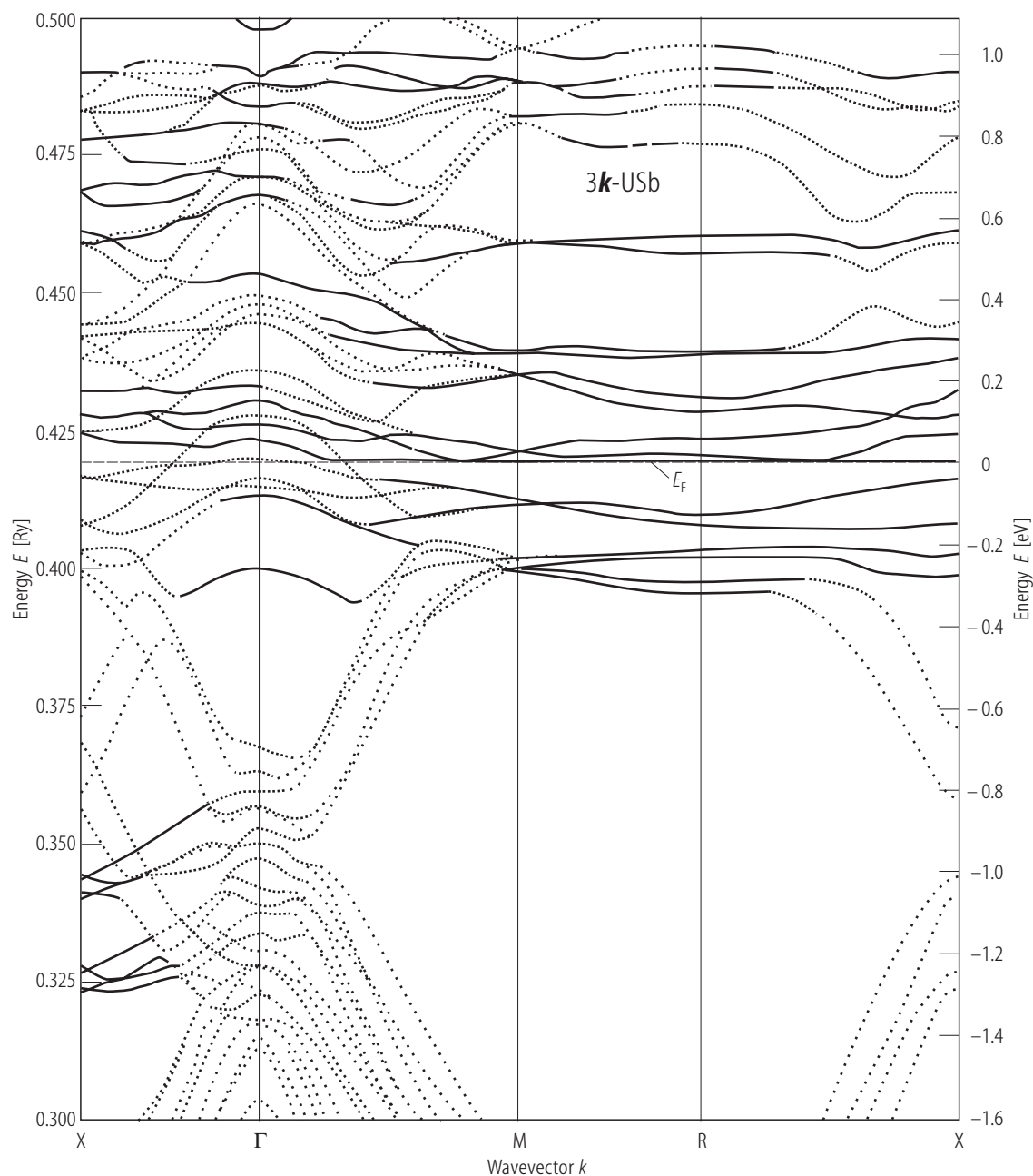


Fig. V.10. USb. The electronic band structure of USb in the vicinity of the Fermi level, calculated by self-consistent fully relativistic non-collinear-spin-polarized R(NC)SP-LAPW method in the antiferromagnetic triple- \mathbf{k} state using the exchange correlation potential in LSDA [99Y], [00Y]. The horizontal dashed line indicates the Fermi level. A fully relativistic formulation of the electronic structure of noncollinear magnets is based on a generalization of the relativistic spin-density functional theory (RSDFT). The

spin p_s and orbital p_l moments are -1.91 and $3.43 \mu_B$, respectively; the total moment p_o is $1.59 \mu_B$. The difference between the total energies of the triple- \mathbf{k} (E_{3k}) and single- \mathbf{k} (E_{1k}) type spin orientation is 2 mRy/mol . Note, that below E_F , the triple- \mathbf{k} band structure has two groups of $5f$ bands at the M points, consistent with the (angle resolved) ARPES [98TKIA] (see Fig. V.20). For the detailed band structure calculation see [00Y].

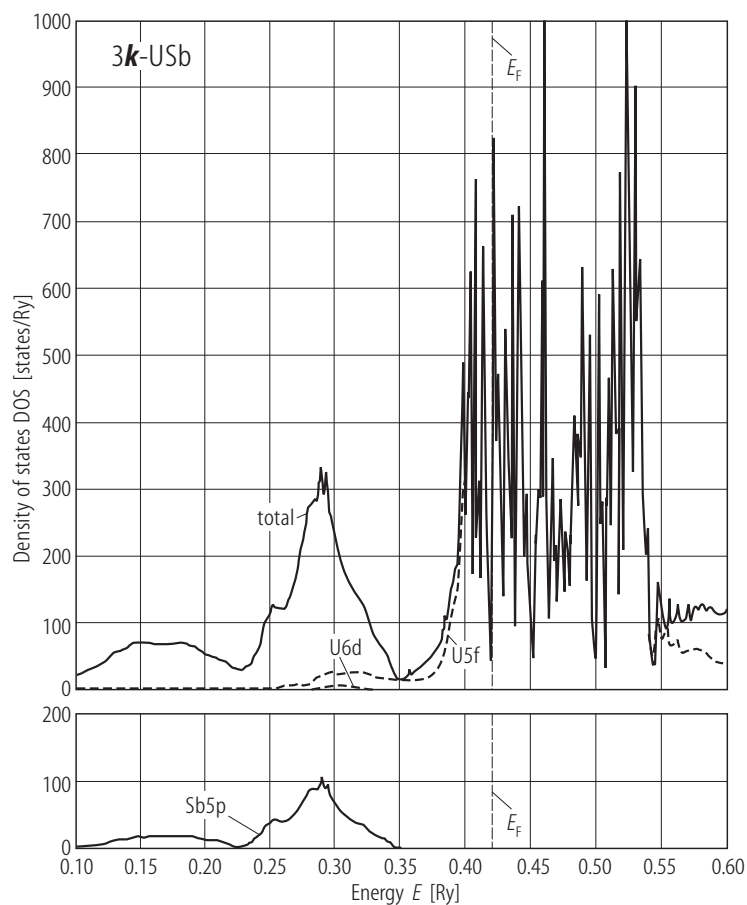


Fig. V.11. USb. DOS in triple- k USb magnetic structure calculated with R(NC)SP-LAPW method [98Y]. The vertical dashed line denotes the Fermi energy E_F . The 6p valence bands are omitted in the Figure. Note that the main 5f bands are located far from E_F and yields a coefficient $\gamma(0) = 4.92 \text{ mJ K}^{-2} \text{ mol}^{-1}$ in agreement with the experimental one ($4.36 \text{ mJ K}^{-2} \text{ mol}^{-1}$ [85ROV2]). This gives also a reasonable interpretation of ARPES [98TKIA] (see Fig. V.20). The total magnetic moment $p_o = 1.52 \mu_B$ is considerably less than the observed value ($2.85 \mu_B$ [80RBQV]).

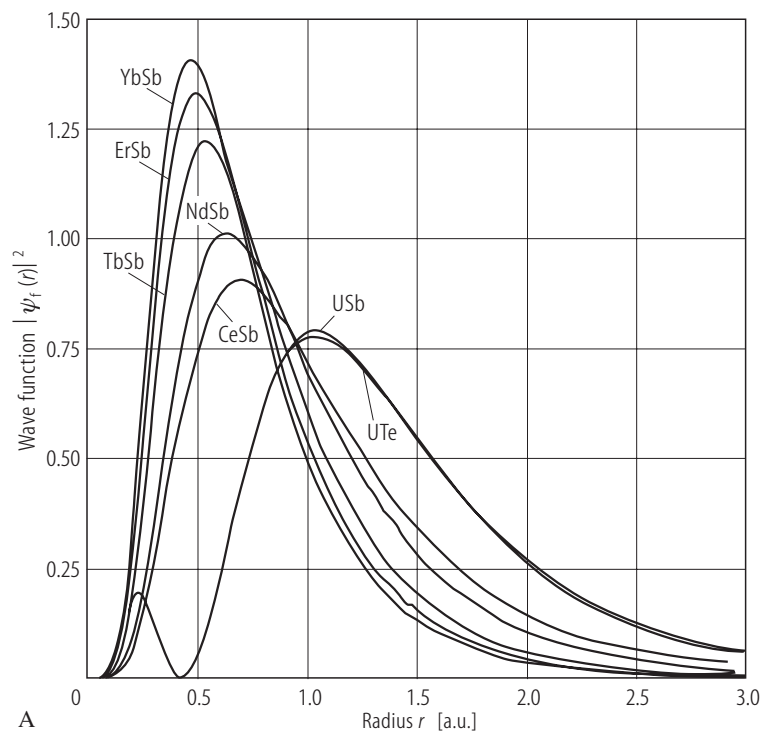


Fig. V.12A. For caption see next page.

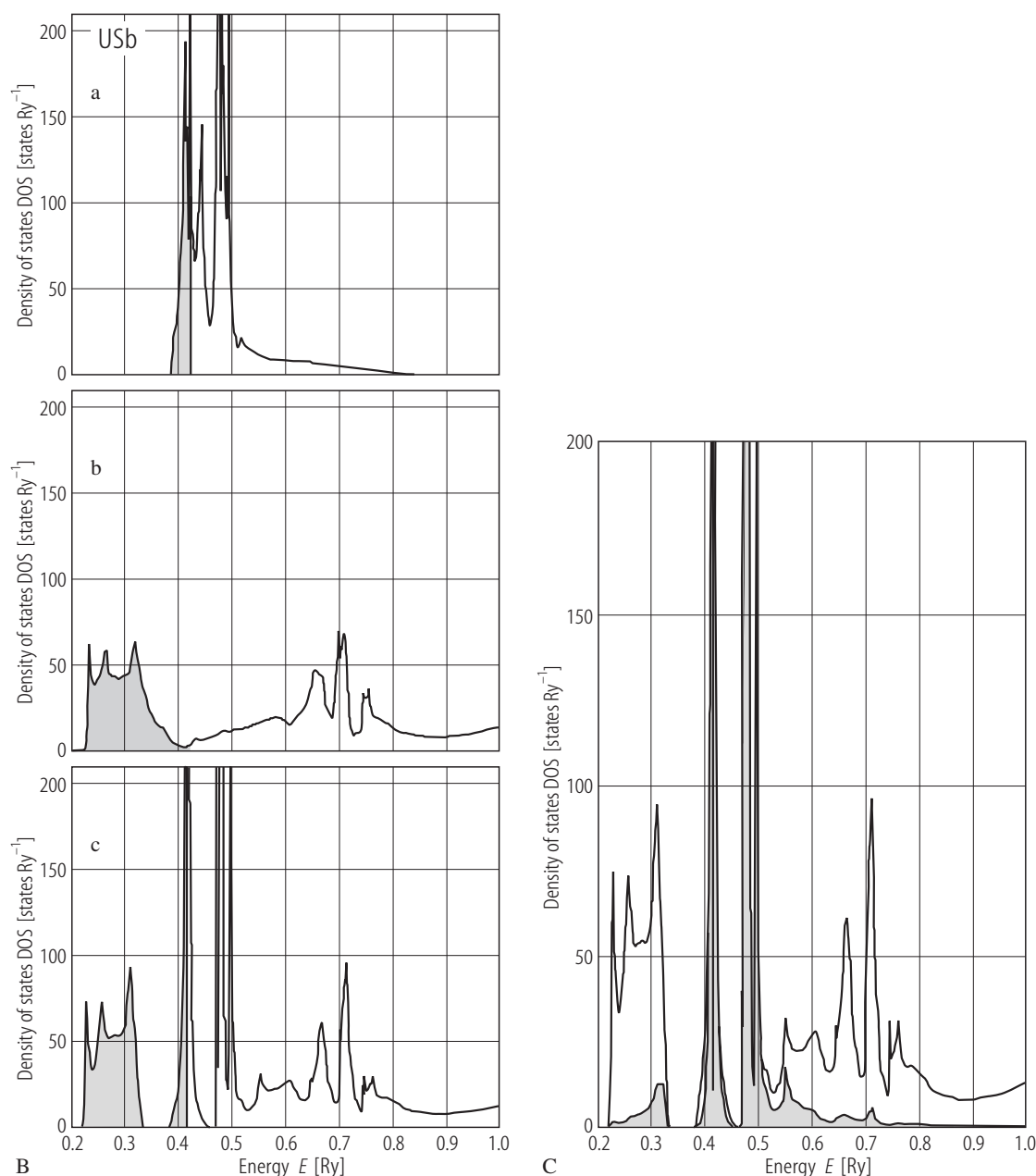


Fig. V.12. USb. **(A)** The f-state squared wave function, $|\psi_f(r)|^2$, vs. atomic radius, r (in atomic units) in comparison to those of RESb (RE = Yb, Er, Tb, Nd, Ce) and of UTe [93CSL] and [93SCL]. The increase in r_{\max} and decrease in the value of maximum of the wave function mark the increase in the degree of f-electron delocalization. **(B)** A comparison of DOS for cases of **(a)** pure f-bands spectrum with non-f states removed from the system, **(b)** the spectrum of non-f bands with f states removed and **(c)** fully hybridized – itinerant spectrum (f states included in the band) [93SCL], [94SCL]. Calculations are based on methods presented in works [87WC], [91SC1] and [91SC2]. In contrast, e.g., to CeSb, the hybridization substantially alters the

unhybridization spectrum (the shaded areas are states below E_F). Note that in **(a)** and **(b)** it is assumed that three electrons belong to the f-band and the remaining electrons belong to the non-f bands. **(C)** Total DOS and $l = 3$ projected DOS [94SCL]. Shading indicates the f-spectrum. It is evident that the 5f-DOS can be represented by the proportion between the spectral weights in the i) f-peak and ii) f-extension. The larger the amount of spectra weight in the f-extension the more itinerant is the system and the reverse. As a result the balance between the two tendencies brought about by (i) and (ii) decides between localization and itinerancy the system lies. Thus this point is reflected by the proportion of the (i) and (ii) spectral weights (the *dual* spectral character of 5f-bands).

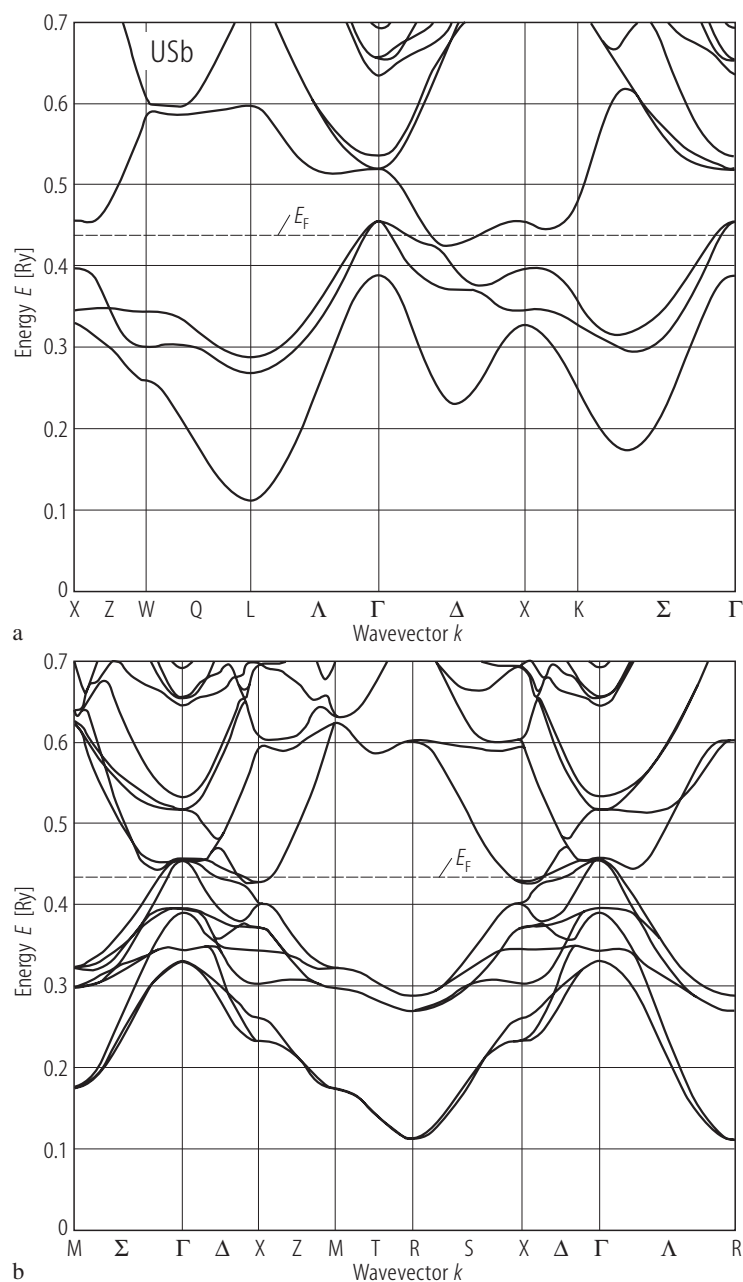


Fig. V.13. USb. Energy band structure keeping U 5f electrons localized, calculated (RLAPW) for a hypothetical compound AnSb corresponding to USb, i.e. having the NaCl crystal structure with **(a)** the body centered cubic (bcc) Brillouin zone and **(b)** the simple cubic Brillouin zone for the AFI – triple \mathbf{k} (see Fig. V.14a) magnetic structure [95HH] and [97IASS]. As compared to LaSb (not shown) the overlap of the actinide d band and the Sb p band is wider because of the smaller lattice parameter of actinide counterpart. For the Fermi surfaces of the hypothetical AnSb see Fig. V.15.

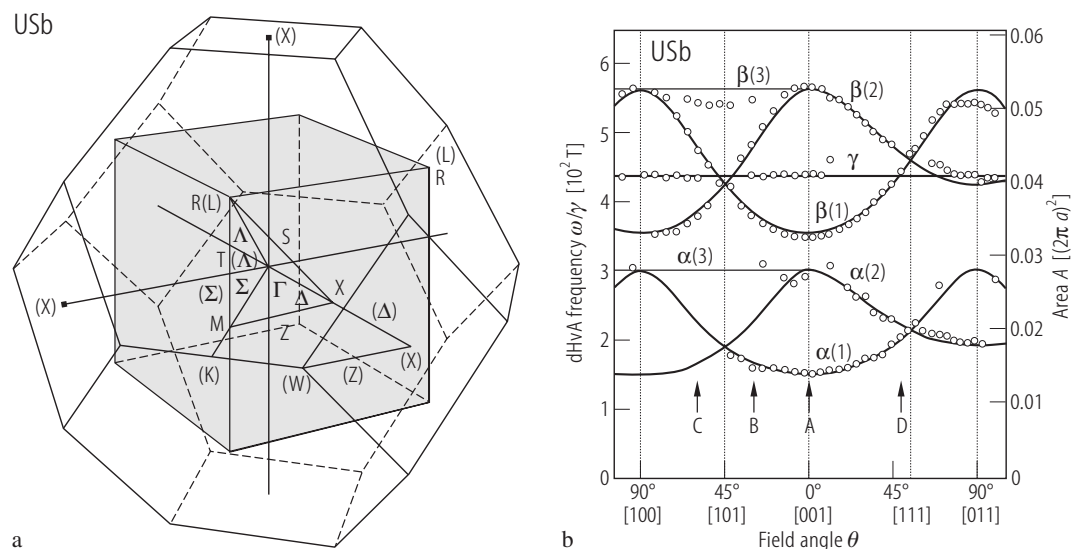


Fig. V.14. USb s.c. (a) The bcc Brillouin zone of the NaCl crystal structure (outside) related to the simple cubic Brillouin zone for the AFI - $3k$ structure (inside) [97IASS]. (b) The dHvA frequencies (left hand scale) at 45 mK and in 7...13.5 T as a function of a field angle, θ , [97IASS]. A is the extremal cross-sectional area (right hand scale) and a is the lattice parameter. Note three branches denoted by α , β , and γ . The first two branches originate from small and large ellipsoidal surfaces respectively, while the latter is a spherical one. By analogy with LaSb [85H] and CeSb [94SGSK] the α - and β - branches are supposed to originate from electron surfaces and the γ -branch

from a hole surface. All three equivalent β -branches were observed, but only two in the case of α -branches. The solid curves represent the calculated results for α and β -branches (ellipsoidal) and γ -branch (spherical). Arrows A...D show the field angles where the effective masses m_{eff} (ranged between 0.9 and 2.7 m_0) were measured. They lead to $\gamma = 2 \text{ mJmol}^{-1}\text{K}^{-2}$. There is, however, the lack of an additional large hole sheet (see Fig. V.15b) to get the experimental value of $\gamma(0)$ ($\approx 4 \text{ mJmol}^{-1}\text{K}^{-2}$). The number of electrons and holes is assumed to be equal, i. e. this is a compensated metal as for a semimetallic material.

For Fig. V.15 see next page

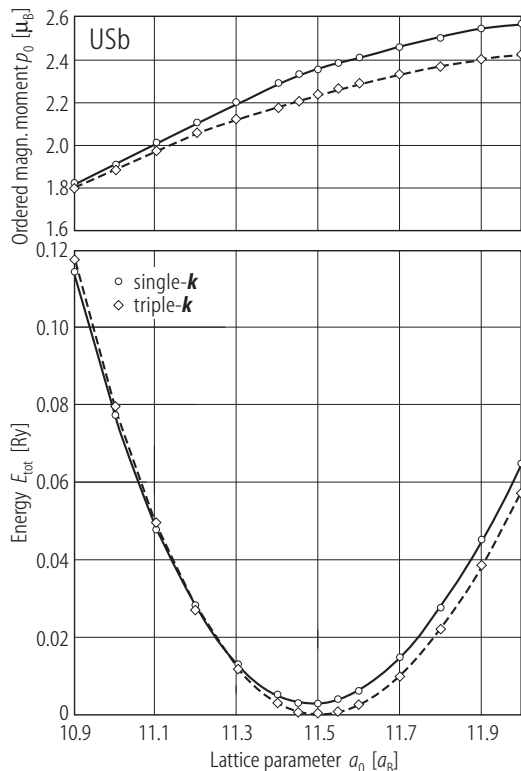


Fig. V.16. USb. The energy E_{tot} and magnetic ordered moment p_0 for single- k (open circles) and triple- k (open diamonds) structures, calculated in the framework of the SDFT as a function of different lattice parameters a_0 [00KS]. Note that the calculated ground state is the $3k$ -structure with a lattice parameter $a_0 = 11.5 a_B$, where a_B is the Bohr radius (experimental value is 11.6993 a_B) [96MGBV]. In turn, the calculated magnetic moment $p_0 = 2.24 \mu_B$ ($p_l = 4.46 \mu_B$ and $p_s = 2.22 \mu_B$) may be compared to the experimental value of 2.85 μ_B and calculated 1.54 μ_B by [00Y].

USb

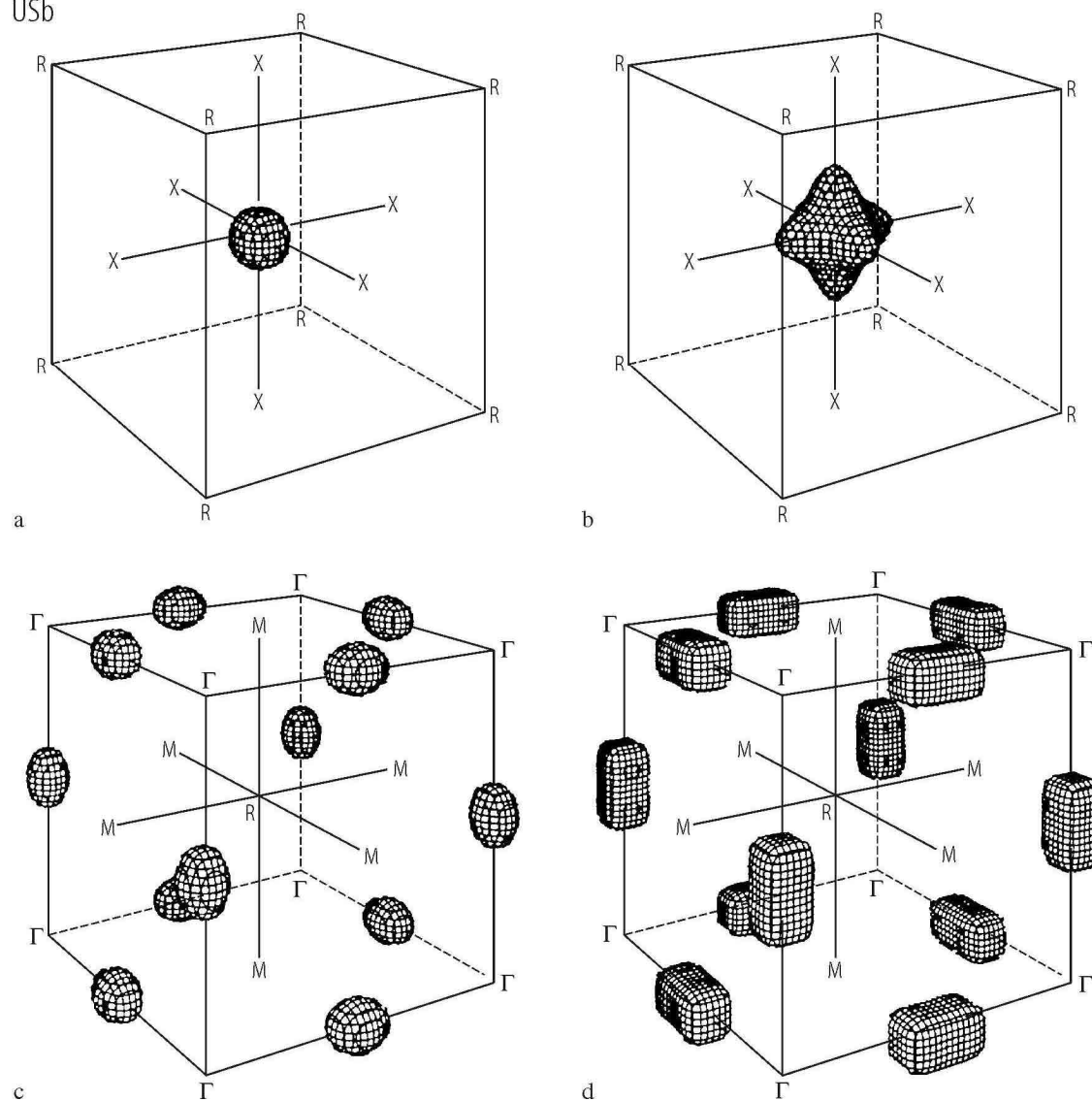


Fig. V.15. USb. Fermi surface of hypothetical AnSb based on the energy band structure (see Fig. V.13) in the simple cubic Brillouin zone for the antiferromagnetic triple- k structure [97IASS], (a) small hole sheet centered at the Γ point, (b) large hole sheet centered also at the Γ point, (c) small electron sheets centered at the X points and (d) large electron sheets centered at the X points.

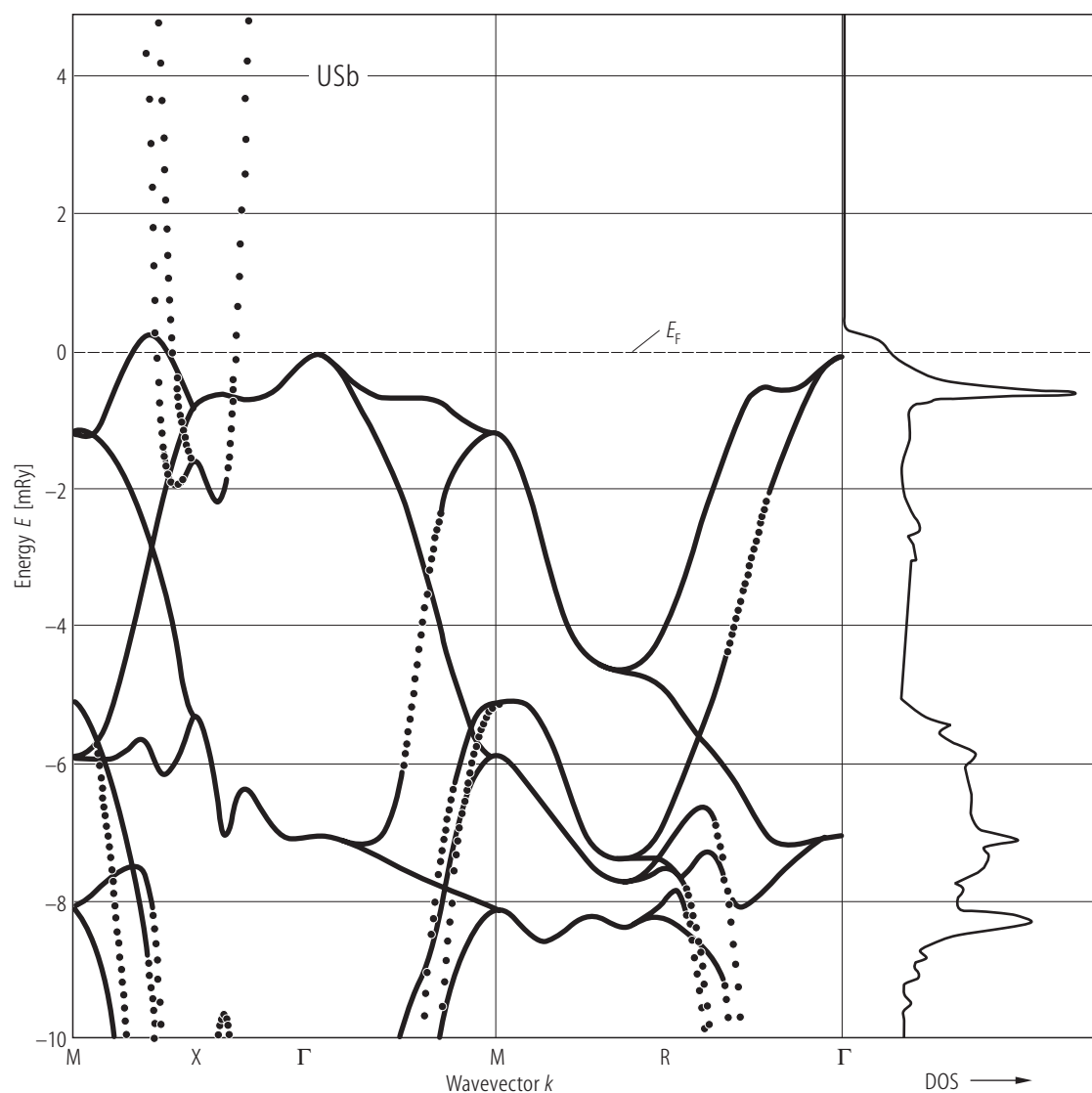
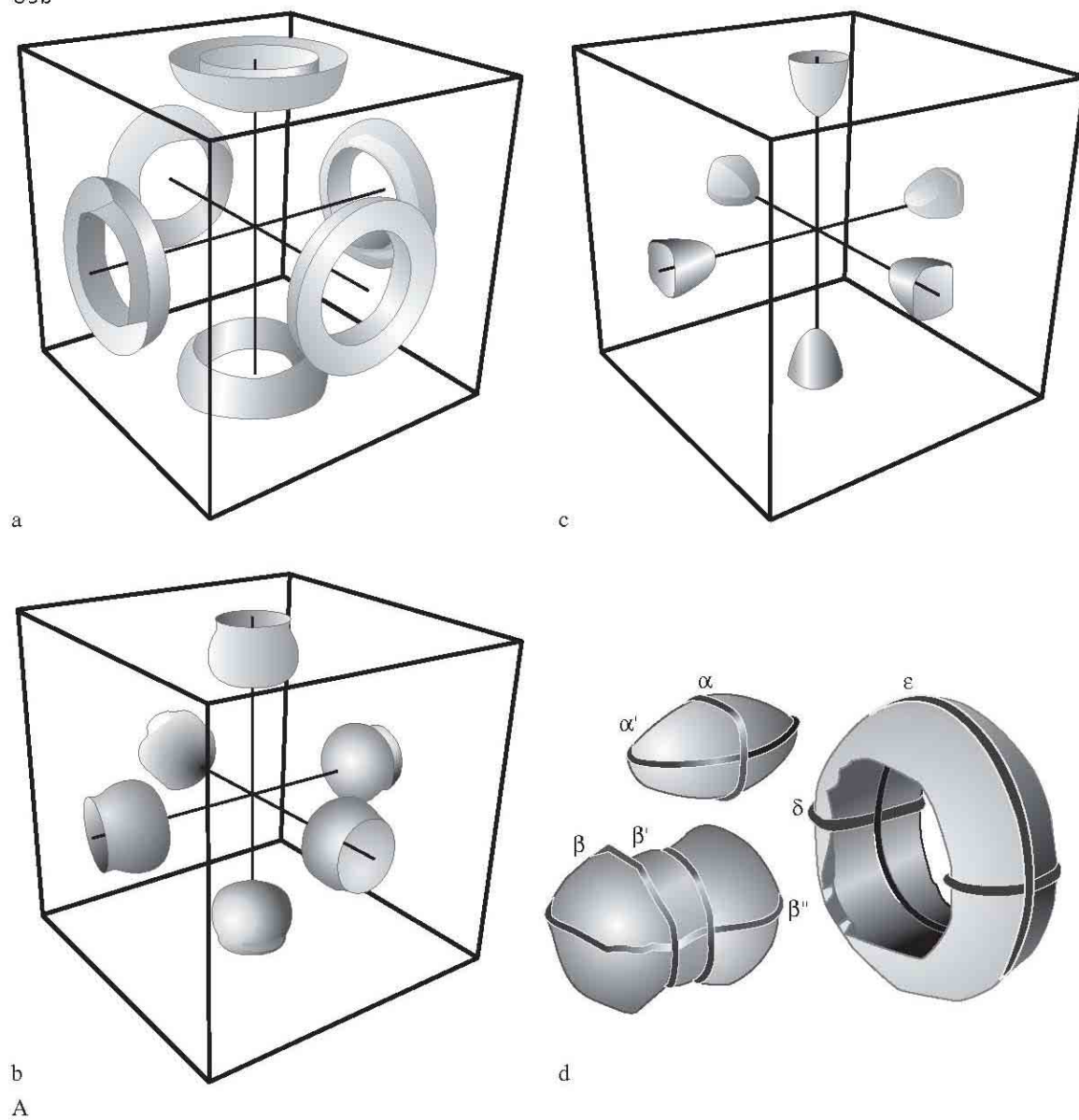


Fig. V.17. USb. Band structure of the multiple- k magnetic structures near E_F (lhs) and DOS (rhs) calculated in the framework of the SDFT theory by using the modified ASW method. Also the full-shape potential and the noncollinearity of the nonmagnetization inside the atomic spheres were taken into account [00KS]. Note the only three

bands crossing E_F , which results in a small number of states at the Fermi level. These bands correspond to three Fermi sheets shown in Fig.V.18A. The theoretical dHvA data compared to such experimental data are displayed in Fig.V.18B.

USb

**Fig. V.18A.** For caption see next page

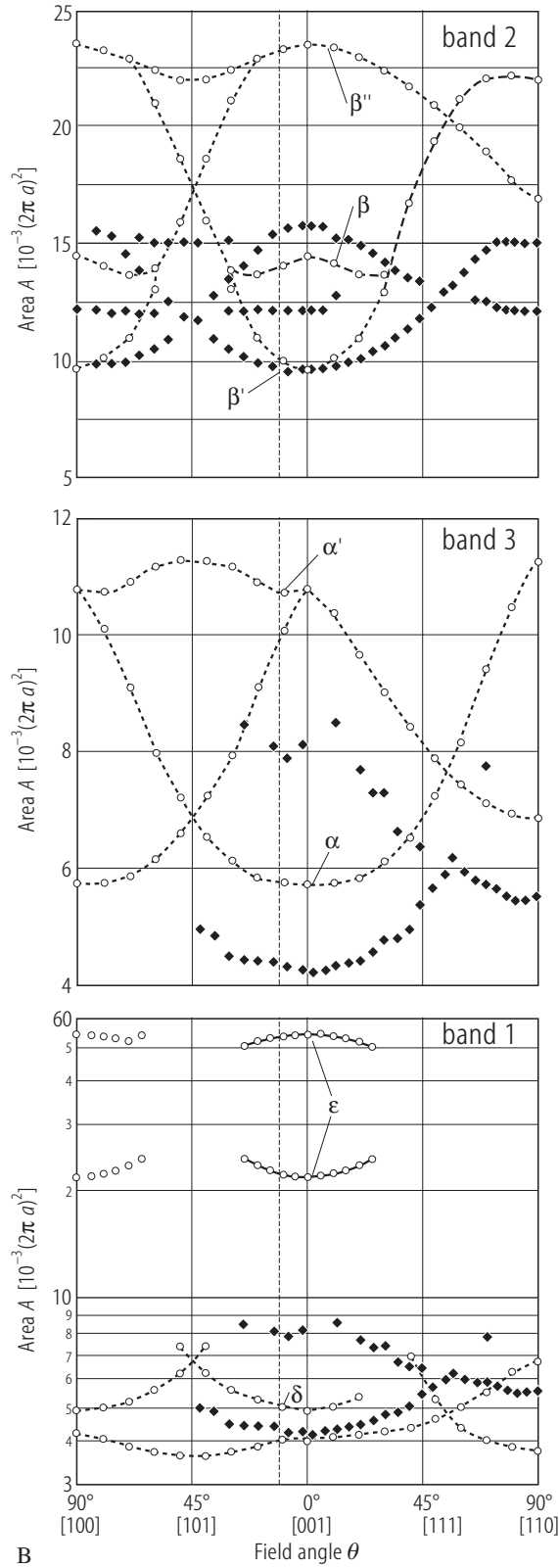


Fig. V.18. USb. (A) The Fermi surface of the triple- k structure [00KS] calculated for the equilibrium lattice parameter $a_0 = 11.5 a_B$ (see Fig. V.16). Band structure SDF calculation leads to the three bands crossing the FL which results in two Fermi surface sheets enclosing holes and consisting of (a) rings centered around the X point and (b) “dog bones”-like sheets centered at the X points, while the third one encloses electron states consisting of (c) cigar-like sheets. (d) The Fermi surface sheets with several extremal cross sections labeled with Greek letters: α , β , δ , and ϵ . Notes: The Fermi surfaces depicted in figure (a) were not found in the experiment (see [97IASS]) and in turn, no spherical sheet at the Γ point, reported in the experiment, has been reproduced by these calculations. (B) Experimental dHvA data (closed diamonds) determined for the triple- k structure [97IASS] compared to the theoretical results (open circles) obtained in this framework of SDF theory within ASA method [00KS]. The system is described by a fully relativistic Hamiltonian including OP correction term. The Greek letters correspond to extremal cross sections of the Fermi surfaces presented in Fig. V.18Ad.

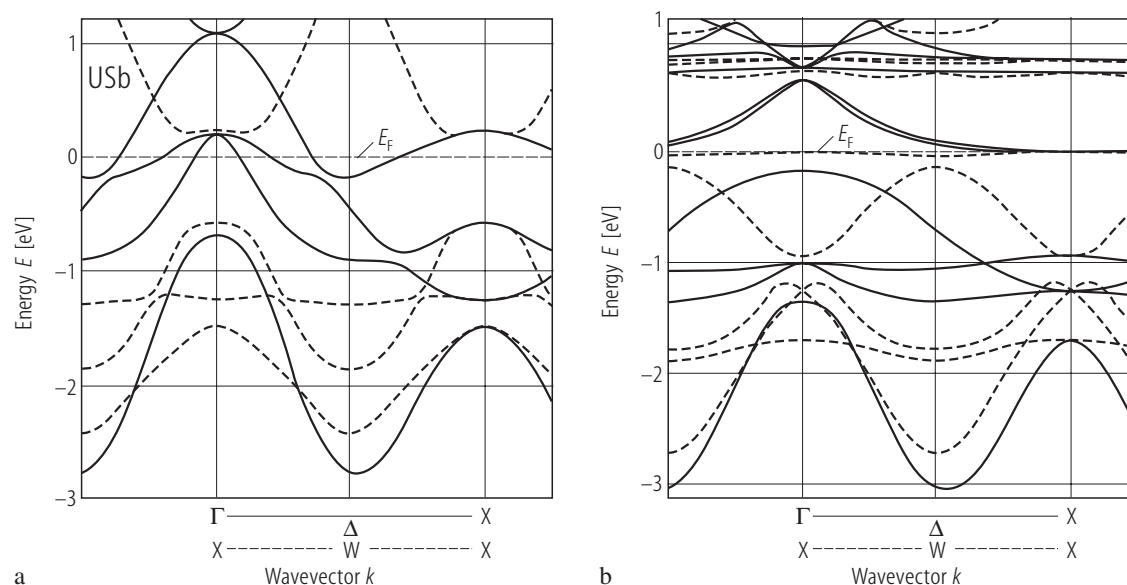


Fig. V.19. USb. Band structures calculated in the framework of LDA with RLAPW method for cases in which: **(a)** U 5f electrons are localized and **(b)** U 5f electrons are itinerant [00KIAH]. The results are obtained for two symmetry lines XWX and Γ X necessary to interpret ARPES results. Good agreement exists between the case **(b)** and the results of [80WP] along the Γ X line. For the case **(a)** the top of the occupied electronic states consists of the Sb 5p states partially occupied, being split into $5p_{3/2}$ and $5p_{1/2}$ bands while the bottom of the unoccupied states are U $6d_{2g}$ ones. The small overlap between the latter states and the $5p_{3/2}$ state would make USb semimetallic like CeSb, but in fact USb is metallic. The essential factor to distinguish the two models is just the location of the Sb 5p bands, which is in agreement with the itinerant model. For the case **(b)** the itinerant model predicts metallic nature of USb (full occupation of the Sb 5p states with binding energies E_b of 1...3 eV according to the ARPES experiment). On the other

hand, there is a full correspondence between these two compounds as to the dispersive Sb 5p bands located at $E_b = (1...4)$ eV in USb and at $(E_F - 3)$ eV in CeSb. In contrast to the localized model **(a)** represented by CeSb there is a lack of hole pockets at Γ points and an electron pocket at the X point (see Fig. V.15). The difference to CeSb makes also the presence for USb (case b) of two dispersionless bands at and just below E_F . The difference in the electronic structure between CeSb and USb is ascribed to closeness of E_F^* to the occupied 5f states in USb compared to the 4f states in CeSb (see the paper for details). The U 5f state being located very close to E_F is expected to exhibit a strong fluctuation with U 6d state also located near E_F . The experimental band structure near E_F is quite different from the calculation based on the itinerant model. Thus the difference in the energy position of the f state causes the drastic difference in the electronic structure near E_F between USb and CeSb.

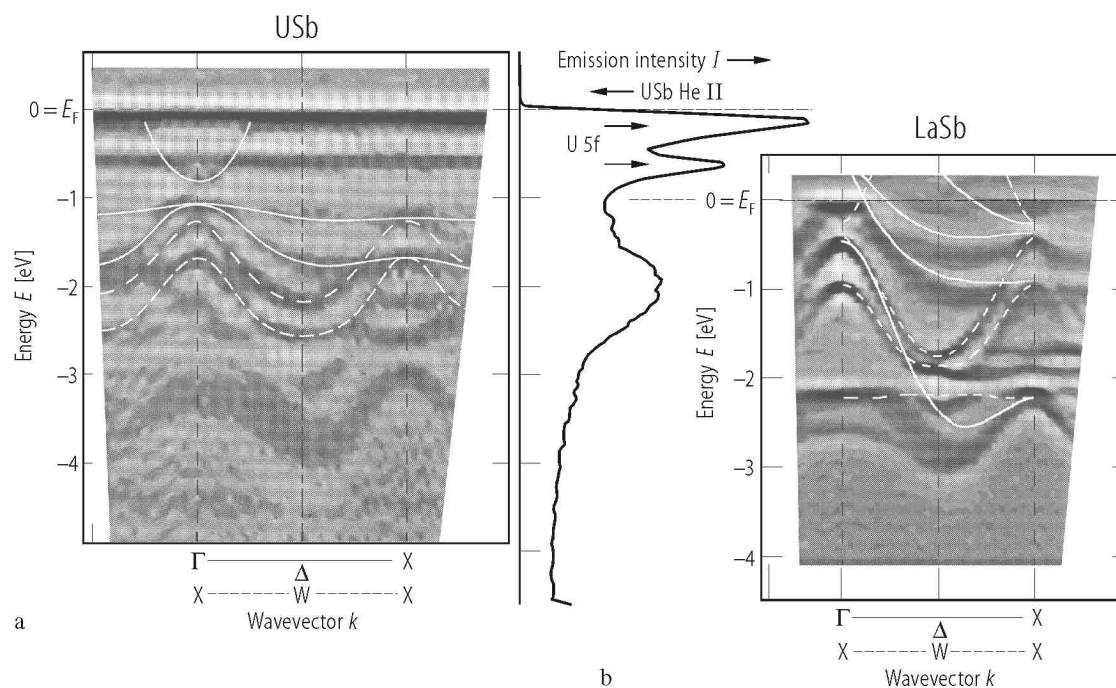
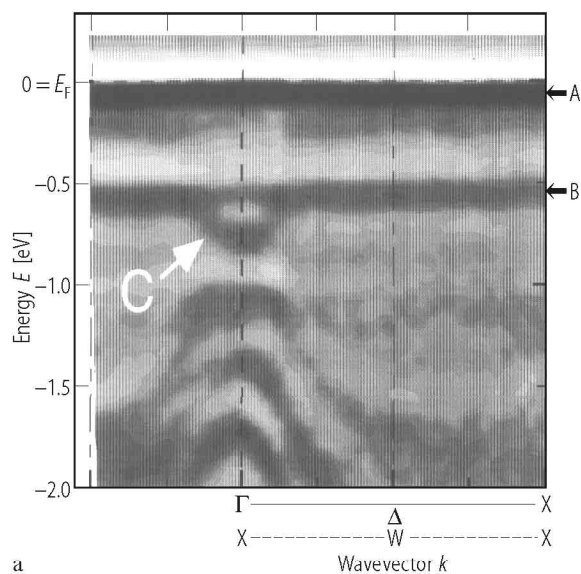


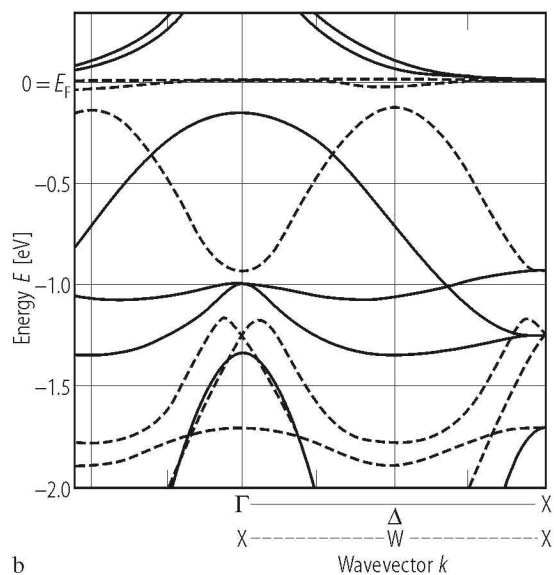
Fig. V.20. USb s.c. Experimental band structures of antiferromagnetic USb **(a)** and LaSb **(b)** derived from the high-resolution angle-resolved photoemission (HR-ARPES) measurements at $T = 25$ K, together with a HR-ARPES He II spectrum of USb (middle panel) [99KKIA]. For comparing the CeSb and USb bands see also [98TKIA] and [00KIAH]. Dark parts correspond to the energy bands. Solid and broken white lines are guides to the eyes and results of band structure calculations for USb and LaSb [85H], respectively. Note two dispersionless peaks with the energy

separation of 0.6 eV and being located near E_F , which may be assigned to the U $5f^2$ final-state-multiplet. The 5f-band closest to E_F forms with the latter a small energy gap of about 10 meV. This is in accordance with the $5f^{3-\delta}$ ($\delta = 0 \dots 0.5$) quasi-localized model [81RMHE]. The dispersive bands being symmetric with respect to Γ , X and/or W points are electron pockets, which may be ascribed to the U 6d band. This indicates a metallic nature of USb in contrast to semimetallic LaSb and CeSb and it is also in contrast to the Fermi surface displayed in Fig. V.15.

USb

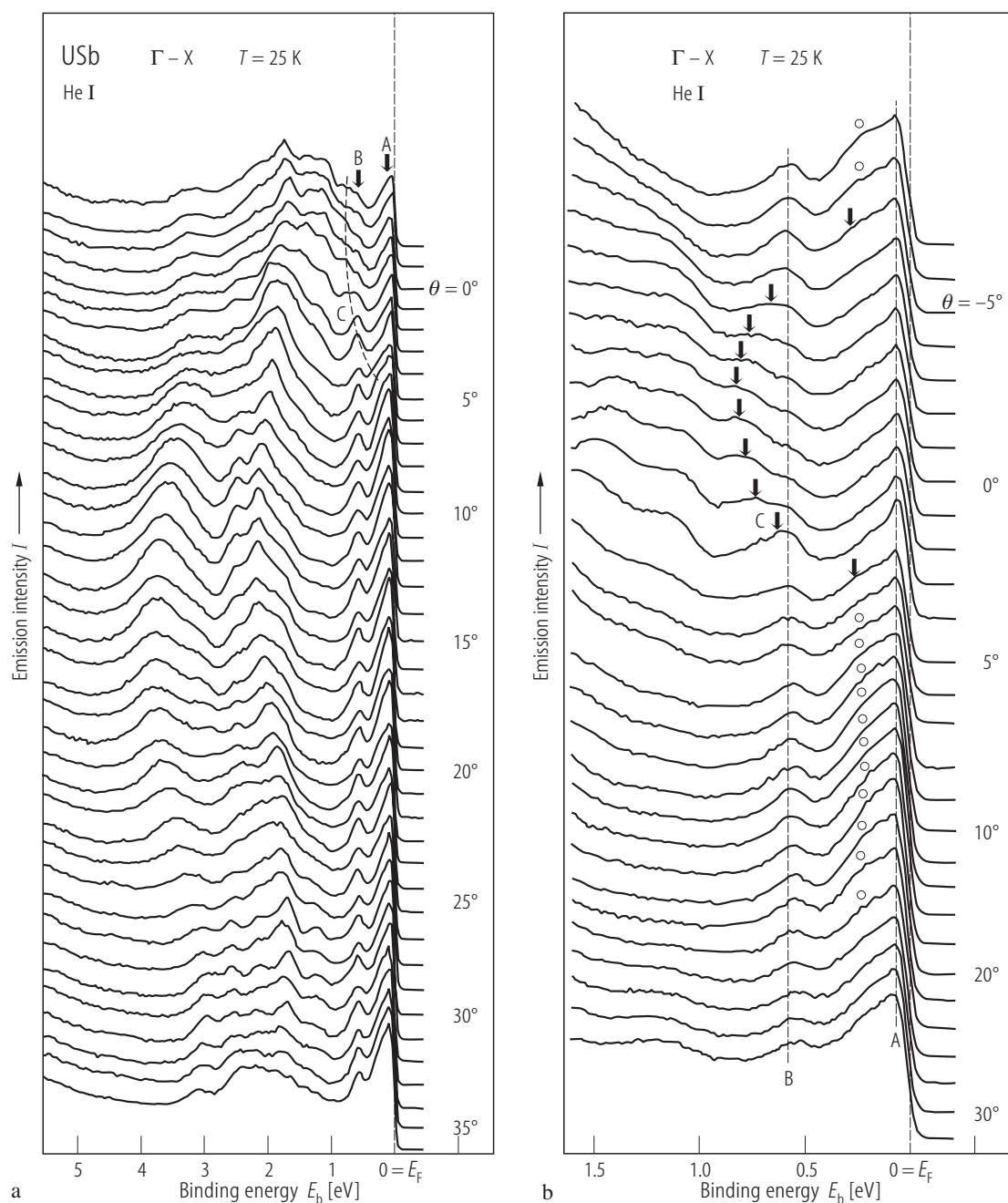


a



b

Fig. V.21. USb s.c. A comparison of (a) the experimental band structure near E_F obtained by HR-ARPES with (b) the band structure calculation based on the itinerant 5f model (case b in Fig.V.19) [00KIAH]. According to this model, the conduction bands near E_F originate in the U 6d-5f hybridized states having strong 5f character at E_F , which is substantially different from the experiment (the U 5f A and B bands are localized non-dispersive bands and located just below E_F). The dispersive band C is ascribed to the U 6d states hybridized with the U 5f states (broken lines in figure b). This self-contradiction found close to E_F between the ARPES spectrum and the itinerant model suggests the existence of a *dual* (itinerant and localized) character of 5f electrons in USb.



A

Fig. V.22A. USb s.c. **(a)** ARPES spectra measured at 25 K (antiferromagnetic state) with the HeI resonance line (21.2 eV) along the Γ -X direction [00KIAH]. The polar angle θ is also denoted. Note two peaks A and B without dispersion, located near E_F . These data are consistent with angle-integrated PES measurements by [81RMHE], [81RMEV], [82RMV], [82RMEA] and [87R2] and with band calculations for the itinerant 5f model (see Fig. V.19). **(b)** The same spectra but near E_F [00KIAH]. Solid vertical

arrows represent the U 5f² final state multiplet. A and B are dispersionless U 5f bands located very close to E_F , and at about 0.6 eV binding energy, respectively, and a small dispersive band C is observed (Γ (X) point in the ARPES experiment). Open circles mark the shoulder of band A seen beyond $\theta = \pm 5^\circ$. The absence of the U 5f states just at E_F (band A does not cross E_F) along the Γ X and XWX directions is consistent with small $\gamma(0)$ -value.

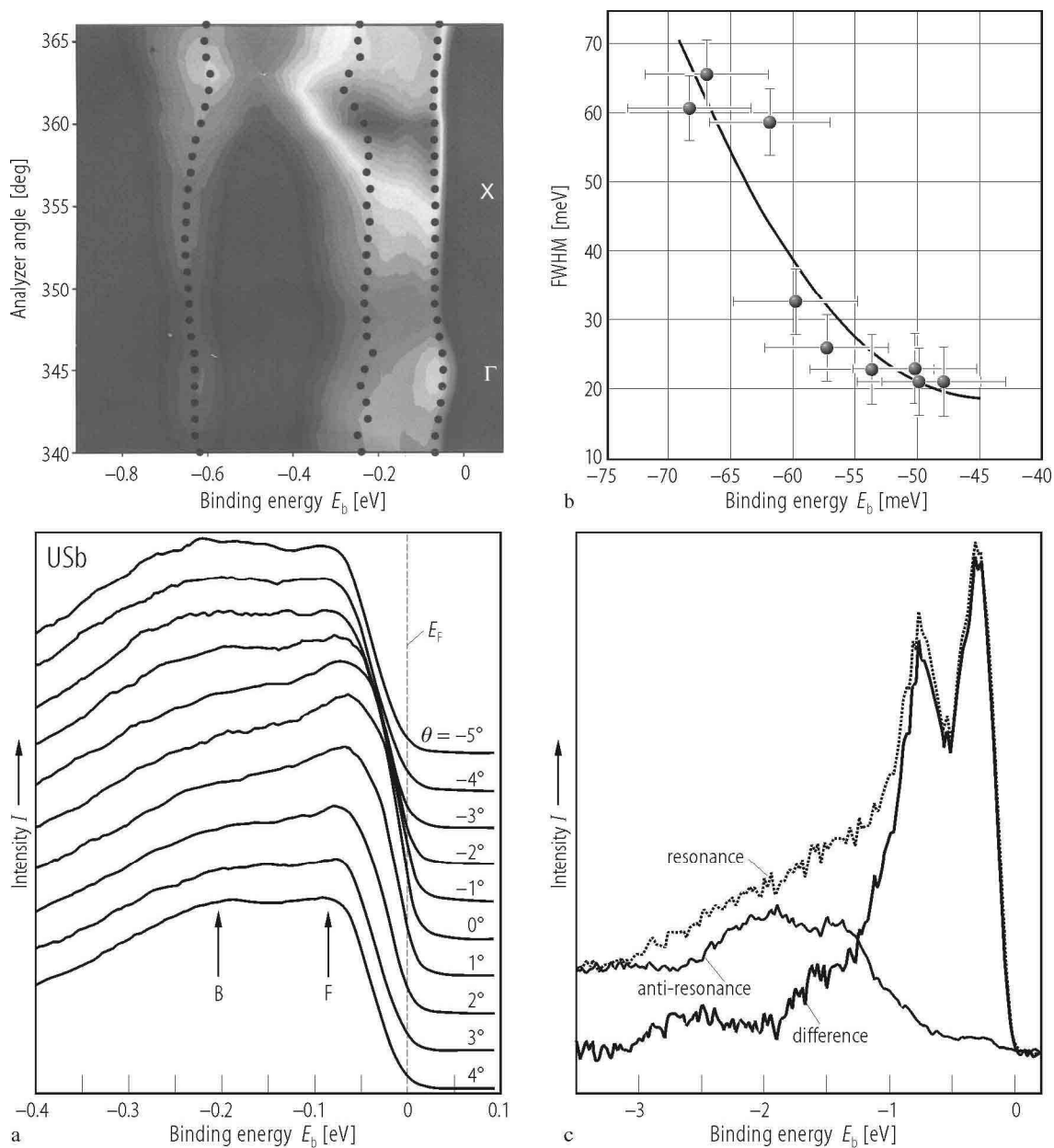


Fig. V.22B. For caption see next page

Fig. V.22B. USb s.c. **(a)** High resolution (25 meV) ARPES data as a function of analyzer angle, θ , [04DJLO]. The following points are noteworthy: i) Peak centered at about 45 meV below E_F displays a significant dispersion between 15 and 60 meV, depending on the crystallographic direction. Dispersions are most clearly seen around the X point. ii) The maximum photoemission intensity is seen away from the high symmetry points. iii) Peak F (closest to E_F) is a band that does not cross E_F . Despite a strong indication of the static and dynamic magnetic data that USb is a localized system there is a strong k -dependence of the valence band spectral weight (see the photograph). The conclusion is similar to that given in [00KIAH] that the 5f states in USb exhibit “dual” character. **(b)** FWHM of the F peak as a function of the BE [04DJLO]. The solid line is a quadrating fitting indicating a conventional behaviour of a dispersive band. The conclusion, which is somewhat in contradiction to less resolved ARPES studies of [00KIAH], is that the peaks B and F represent some dispersive narrow 5f bands, not crossing E_F . **(c)** Resonance scans taken at a photon energy of 95.75 eV and anti-resonance at 91.25 eV [04DJLO]. The difference data confirm a dominating 5f character of this band within the first eV of the spectrum. It is concluded that the first 5f: $4I_{9/2}$ term is predicted at 500 meV. However, the multiplet transition $4I_{9/2} \rightarrow 4I_{11/2}$ should show, in opposite to the experiment, no dispersion. It is suggested that one out of the three final levels may be associated with the 2F_2 term in accordance with multiplet theory. - Photo caption: Angular resolved photoemission study on single crystalline USb. Data taken in the Synchrotron Radiation Center, Wisconsin, USA, on the PGM branchline with 20 meV of electron energy resolution. Note dispersions of the first three 5f-character peaks (opposite to UTe).

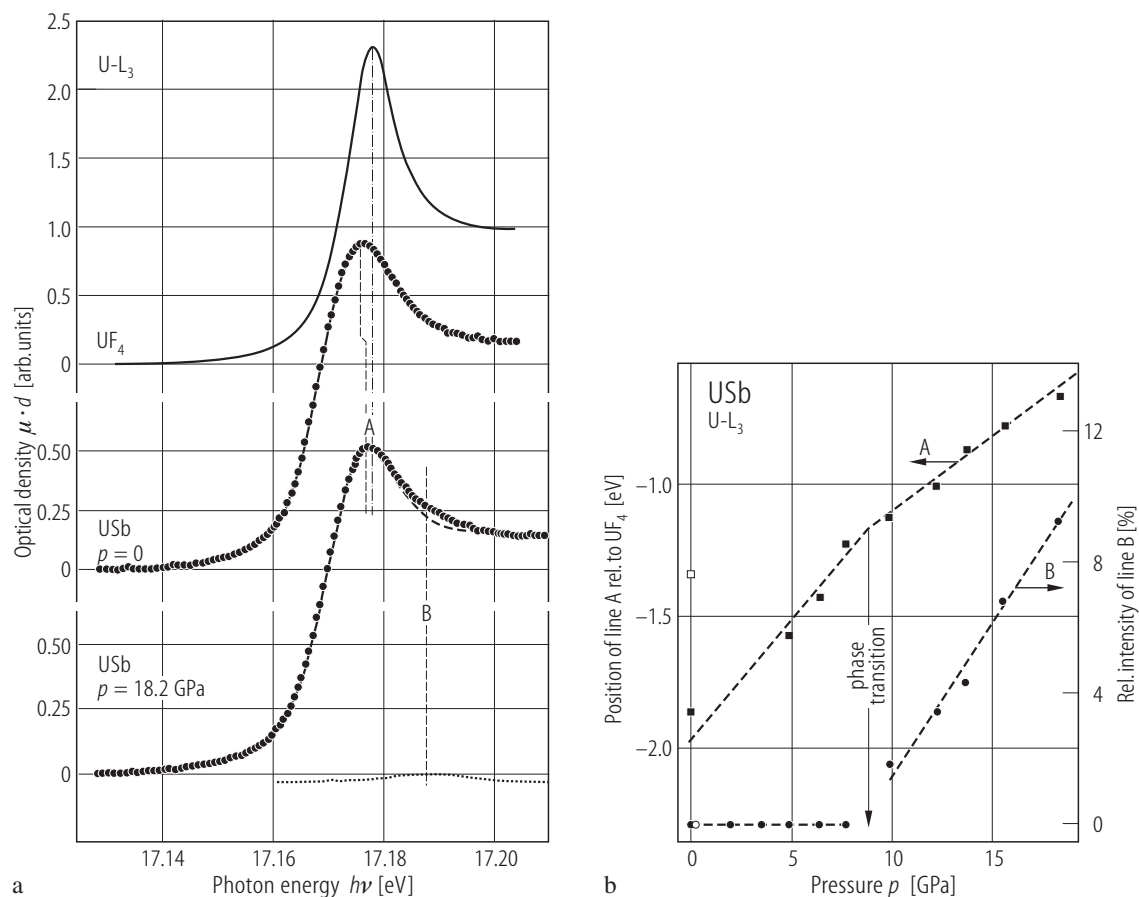


Fig. V.23. USb. **(a)** L₃-edge XA spectra at RT measured at ambient pressure and at 18.2 GPa compared to the reference spectrum of UF₄ [87SBKV]. Note the pressure-induced shift of the white line A to higher energies as a result of a decrease in the 5f electron occupation number according to theoretically predicted result [84B2]. A relatively weak and 16 eV-broad satellite B is observed due to the high-pressure CsCl-type phase formed above 8 GPa [86VORL].

(b) Relative (to UF₄) position changes of line A (left-hand scale) and a relative intensity of line B (right hand scale) as a function of pressure [87SBKV]. The vertical arrow points to the NaCl \Rightarrow CsCl transition, while the open symbols mark the results after pressure release. The B-line is due to a multiple-scattering resonance in the U-Sb covalent bond observed only for the CsCl-phase. Covalence of the U-Sb bonding in this phase increases with pressure.

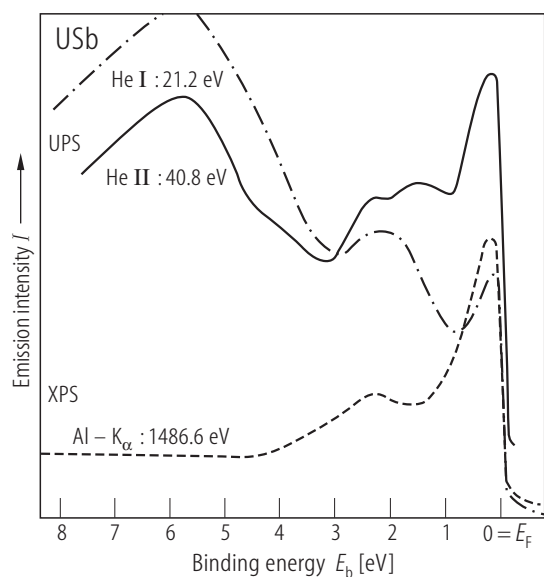


Fig. V.24. USb s.c. Valence band investigation by comparison photoemission spectra for different excitation energies (UPS and XPS) [79BNB]. Note that the UPS spectra show an additional strong and broad (about 4 eV FWHM) emission at -5.5 eV. Possible surface oxidation did not permit unambiguously to identify the emission at -2.2 eV and -5.5 eV. (See LB III/12c, p.431, Fig. 52).

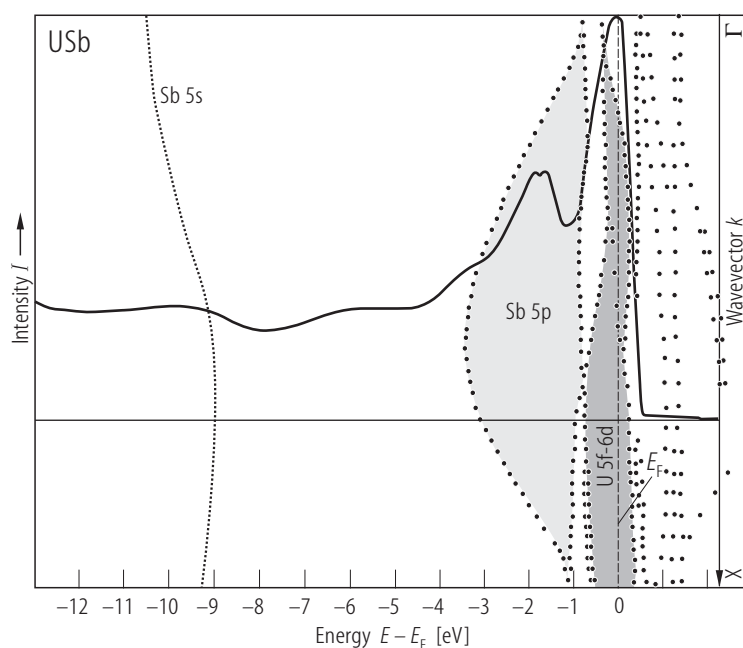


Fig. V.25. USb s.c. ARPES-EDC spectrum taken at $h\nu = 45$ eV (solid line), which is superimposed on an electronic band (dotted lines) calculated along the Γ -X (100) direction of the fcc BZ [80BBBP]. The band structure was determined self-consistently by LMTO method in ASA. Note that bands located just below E_F are flat in accordance with other calculations (see e.g. Fig. V.10).

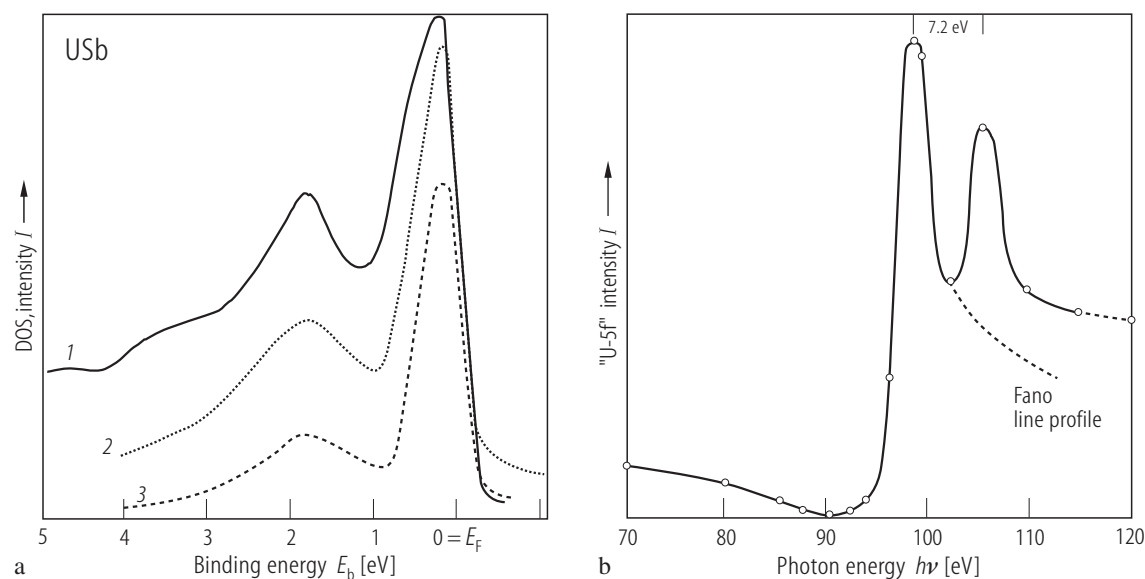


Fig. V.26. USb s.c. (a) Experimental (ARPES) spectrum (1) is compared to one-dimensional total DOS (2) convoluted with a Gaussian (FWHM = 0.2 eV) as the instrumental resolution and with Lorentzian (FWHM ~ 0.8 ($E - E_F$)) in order to take into account lifetime effects. This is further compared to one-dimensional partial ($l = 3$) DOS (3) [80BBBP]. (b) A Fano-type resonance; constant initial state

spectrum of the “U-5f” peak between 70 and 120 eV in the range of the 5d – 5f excitation (open circles). Solid line is a fit using a Fano profile with the parameters: resonance energy $E_0 = 98$ eV, line shape parameter $q = 2.2$ and half width $\Gamma = 3.5$ eV [80BBBP]. The experimental double peak corresponds to excitation from the 5d spin-orbit components (E_b of (5d, 5/2) level is 95.7 eV).

For Fig. V.27 see next page

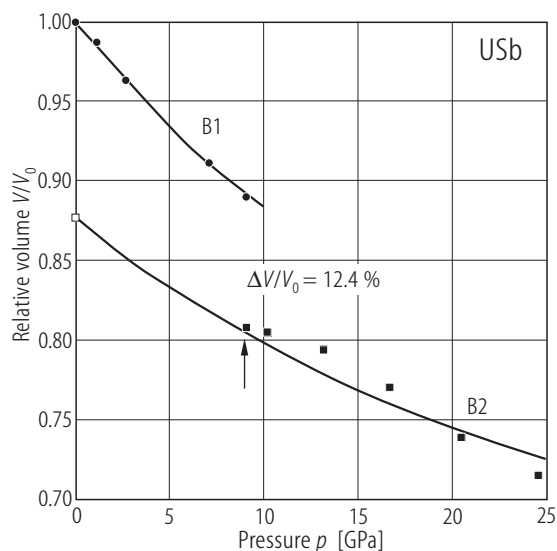


Fig. V.28. USb. Relative volume, V/V_0 , vs. pressure, p , up to 25 GPa [89SGBD]. B1: fcc NaCl-type structure, B2: primitive cubic CsCl-type structure. Full symbols: increasing pressure, open symbol: decreasing pressure. The solid curves were calculated from the equation of state. The B1-B2 phase transition takes place at ~ 9 GPa with a 12.4 % volume collapse as compared to that of 9.2 % (11.8 % at normal pressure) reported by [86VORL] at 8 GPa. However no such transition is predicted by calculations up to 100 GPa (see [97JS]).

Note that the B1-B2 transition has a considerable hysteresis. The B2-phase X-ray lines are present all the way down to zero pressure. Thus, the lattice parameter a_0 of the B2 structure (CsCl-type) is equal to 0.3732(8) nm at RT. The bulk modulus B_0 and its pressure derivative B_0' are given in Table 6. See also Fig.R. 7A.

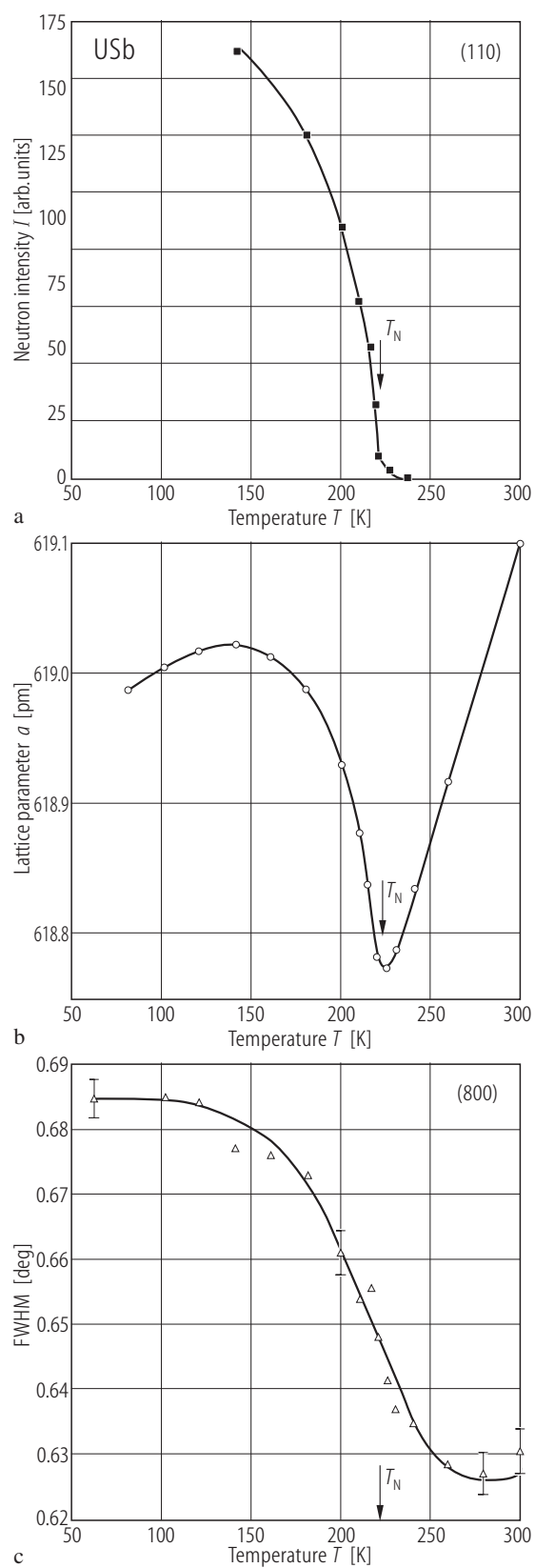


Fig. V.27. USb s.c. The temperature dependence of **(a)** neutron intensity I (110), **(b)** lattice parameter a and **(c)** FWHM ((800) reflection) around T_N ($= 220.6$ K) [80KLMV]. The initial thermal expansion coefficient $\alpha \sim 7 \cdot 10^{-6}/\text{K}$.

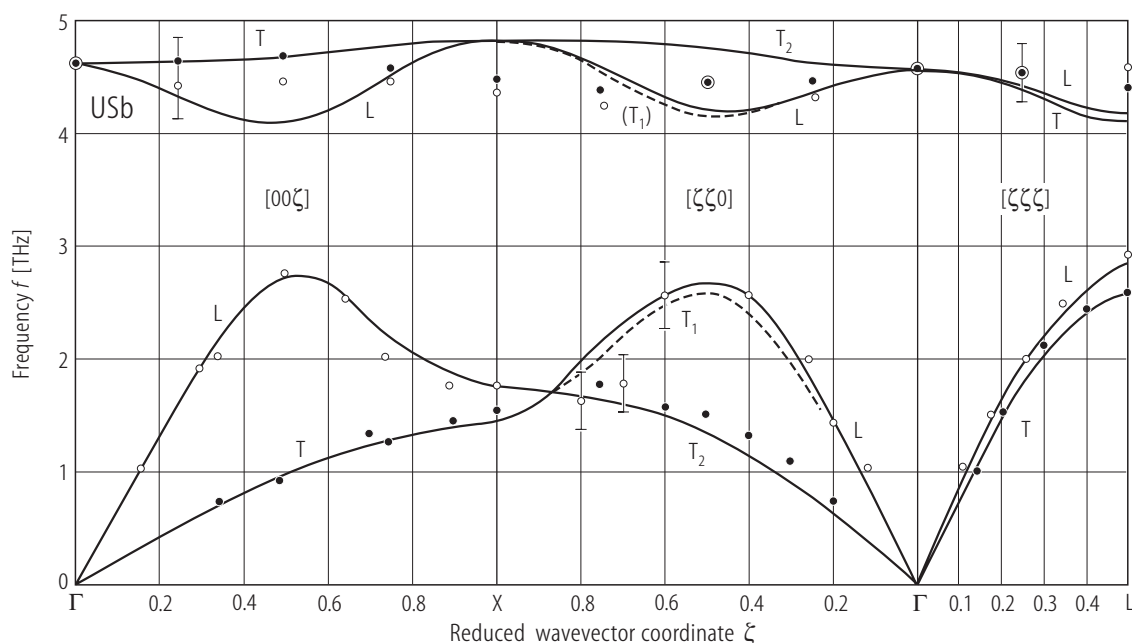


Fig. V.29. USb s.c. Phonon dispersion curves (PDC) [83SLV]. Open and closed circles are longitudinal (L) and transverse (T) modes, respectively. Solid curves are best fits to simple lattice dynamical models, based on six parameters (U–X, X–X, U–U, for both radial and tangential forces) of the conventional Born – von Kármán model, identical to that used by [71SG] to describe the lattice vibrations in UC (see Fig. I.30). The dashed curves are the prediction of the model (see the original paper). Note the near degeneracy of the [110] acoustic TA and LA modes ($f_{LA} > f_{TA}$) at the X

point of the BZ. However no splitting of the optical TO and LO modes at the zone center Γ occurs. From the initial slopes of the acoustic phonon branches the following elastic constants for USb were found: $c_{11} = 1.60(10)$, $c_{44} = 0.20(10)$ and $c_{12} = 0.07(15)$ – (all in 10^{12} dyn cm $^{-2}$). Similar results were reported also for UAs (see Fig. IV.15). See also Table 9. For the calculated PDC's using a three-body interaction rigid-model with seven parameters see [92JS]. However, the model reproduces only some features of the PDC's.

For Fig. V:31 see next page

USb

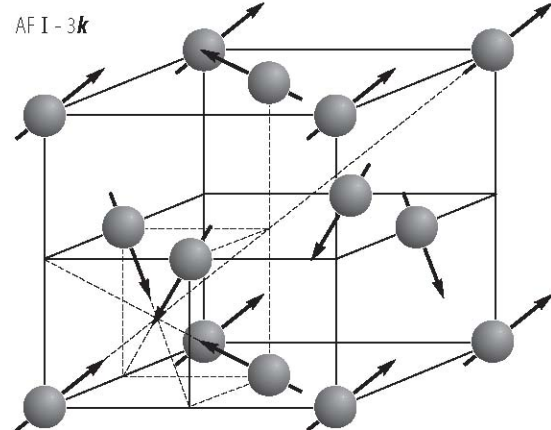


Fig. V.30. USb. Magnetic structure of the AF I – $3k$ -type, taken from [02NSML1]. The compounds with this magnetic structure have a high ordering temperature and the largest R-correlation value. It means that the strong magnetic interactions stabilize this type of structure. For references see [91LA].

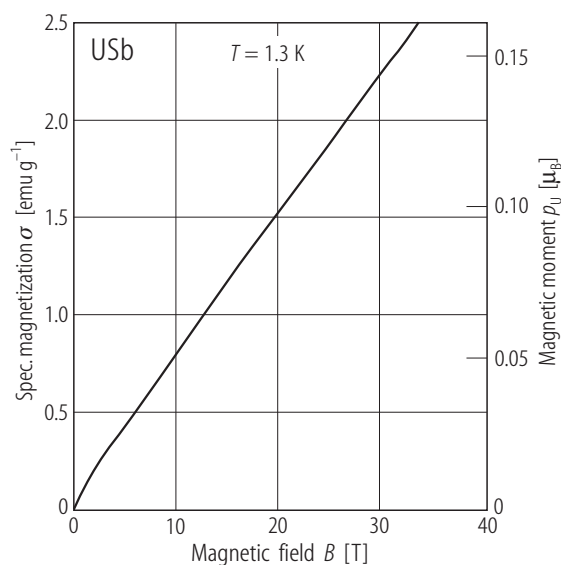


Fig. V.32. USb. Specific magnetization, σ , vs. applied magnetic fields up to 35 T at 1.3 K [78ST]. $a_0 = 0.6208(9)$ nm, $T_N = 213$ K. The high-field susceptibility $\chi_{hf} \approx 7.2 \cdot 10^{-6}$ emu/g at 1.3 K is in accordance with single crystalline susceptibility data.

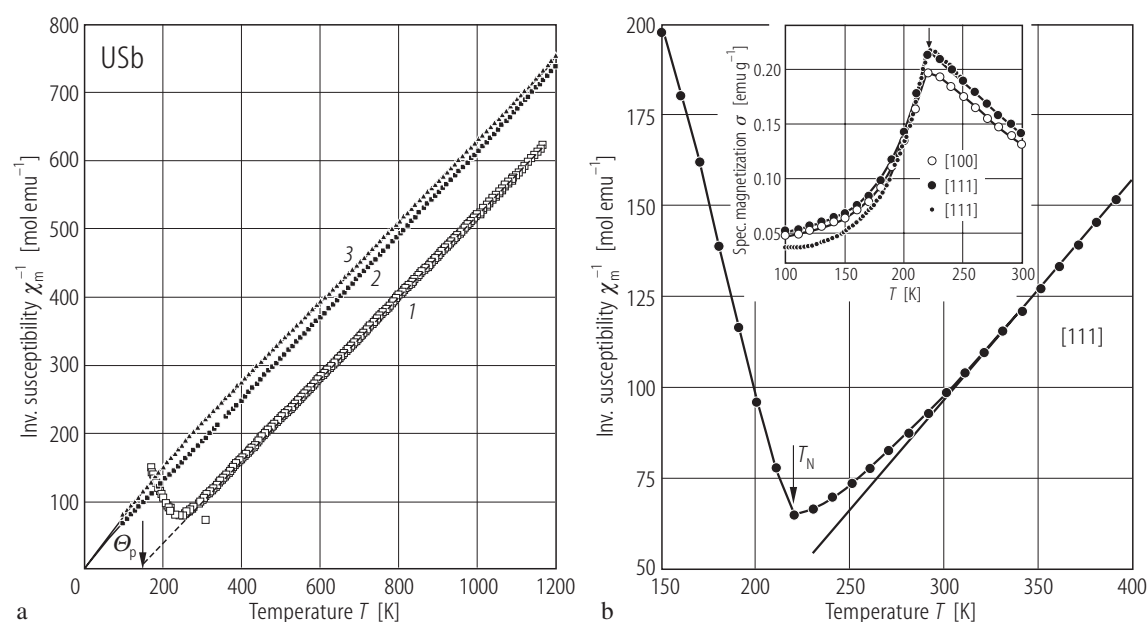


Fig. V.31. USb, sc. **(a)** 1) Experimental results (open squares) of inverse molar magnetic susceptibility, χ_m^{-1} , vs. temperature, T , up to 1200 K [79BHV], compared to such a dependence calculated on the basis of 2) CEF field parameters found from the form factor behaviour (closed squares) [76LMSV] and 3) from the random-phase approximation (RPA) of the magnetic excitation spectrum which provided also information on the crystal field interaction (closed triangles) [86HF]. Calculation of χ_m^{-1} vs. T curve was carried out by [03G]. The quartet $\Gamma_8^{(1)}$ is the ground state, the doublet Γ_6 and quadruplet $\Gamma_8^{(2)}$ are the excited states. Very similar results to those presented by

curve (2) are obtained for CEF parameters of [85TC]. **(b)** Inverse molar magnetic susceptibility, χ_m^{-1} , vs. temperature, T , measured up to 400 K along the magnetization easy axis [111] and hard axis [100] [05TSMC]. T_N (≈ 220 K), $\Theta_p = 138$ K, $p_{\text{eff}} = 3.6 \mu_B$, which are compatible with the high-temperature data [79BHV] shown in figure **(a)** ($\Theta_p = 140$ K, $p_{\text{eff}} = 3.64 \mu_B$). For comparison, the [111] data of Ref. [02NPSM] are given in the inset (small full circles) where the magnetization, σ , against temperature is shown at $B = 0.5$ T. The deviation in the results below T_N may be caused by the difference in the presence of impurities, especially of ferromagnetic U_3Sb_4 ($T_C = 146$ K).

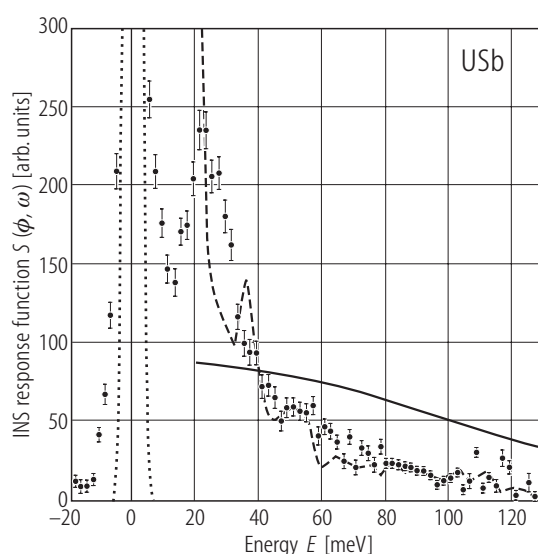


Fig. V.33. USb. The high-energy magnetic spectrum, measured in the low-angle detector bank used in the pulsed neutron source ISIS (U.K.) [88OHJS]. The data were transformed from TOF to energy transfer. Incident neutron energy $E_i = 150$ meV applied at 20 K. Dotted line – elastic scattering, dashed line – phonon spectrum in the high-angle bank, solid line – predicted model of crystal field scattering according to [85HV] and [86HF]. No crystal field excitations have been detected. The peak at 26 eV can be correlated with the “flat” spin wave branch [80LS] and [85HV] (see Fig.V.42).

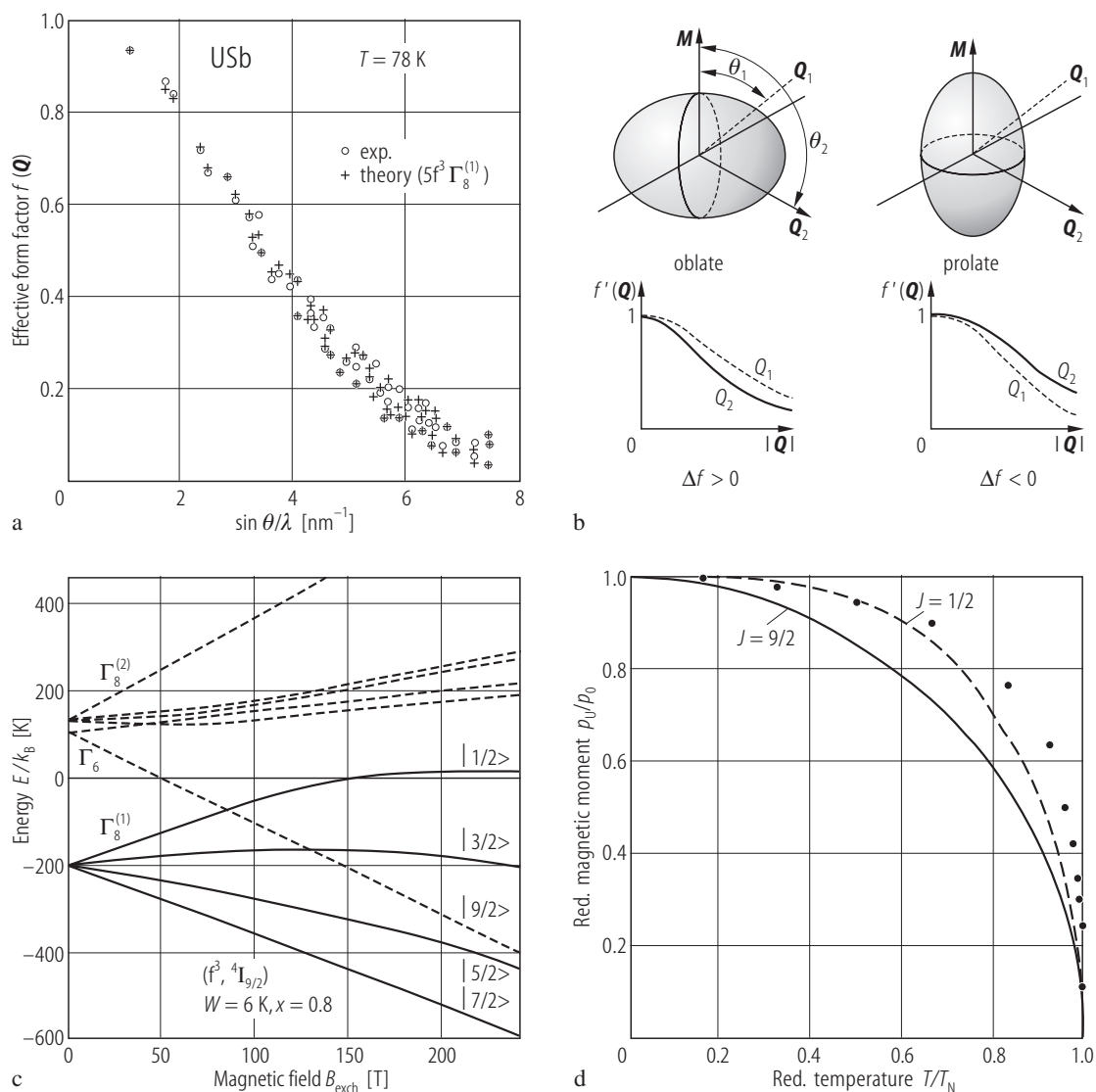


Fig. V.34. USb s.c. **(a)** Effective magnetic form factor $f(Q)$ observed (open circles) and calculated (crosses) as a function of scattering vector $Q/4\pi$ ($= \sin \theta/\lambda$) [76LMSV]. The magnetic cross section was calculated with the tensor-operator method. The calculations favour the magnetization density of ground state to be *oblate* (see figure **(b)**) and the major component of the wave function to be $|M = 7/2\rangle$ which corresponds to the $\Gamma_8^{(1)}$ quartet as being a ground crystal field level. This implies that the LLW-parameters should be as $x > 0$ and $W > 0$ (see LB III/12c, p.430, Fig. 46). **(b)** A ground state in USb from the form factor analysis. Schematic representation of magnetization densities (upper plot) and magnetic form factors $f'(Q)$ (lower plot) for two cases: *oblate* and *prolate* electron densities. The experimental data ($\Delta f > 0$) point to the *oblate* density, i.e. the quadrupole moment is compressed along the direction of

moment M . Also the triple- k structure with a $[111]$ direction of moments is consistent with the form factor analysis. **(c)** The crystal field level scheme with an external field B_{exch} , using a molecular field model [76LMSV]. In the absence of B_{exch} the $\Gamma_8^{(1)}$ - Γ_6 energy separation was established to be about 300 K. On the basis of the form factor analysis the coefficient of the molecular field λ was found to be $92 \text{ T}/\mu_B$, which leads to $T_N \sim 280 \text{ K}$ and $\Gamma_8^{(1)}|M = 7/2\rangle$ as a ground state. The higher experimental p_0^{exp} ($= 2.82 \mu_B$) than calculated p_0^{calc} ($= 2.51 \mu_B$) moment results from the population of $\Gamma_6|M = 9/2\rangle$ level at high B_{exch} value ($\sim 220 \text{ T}$). **(d)** The reduced magnetic moments $p_U(T)/p_0$ as a function of reduced temperature T/T_N [76LMSV]. $p_0 = 2.82 \mu_B/\text{U at.}$, $T_N = 241.2(1) \text{ K}$. The solid and dashed curves give Brillouin functions for $J = 9/2$ and $1/2$, respectively, (see also LB III/12c, p.430, Fig. 47).

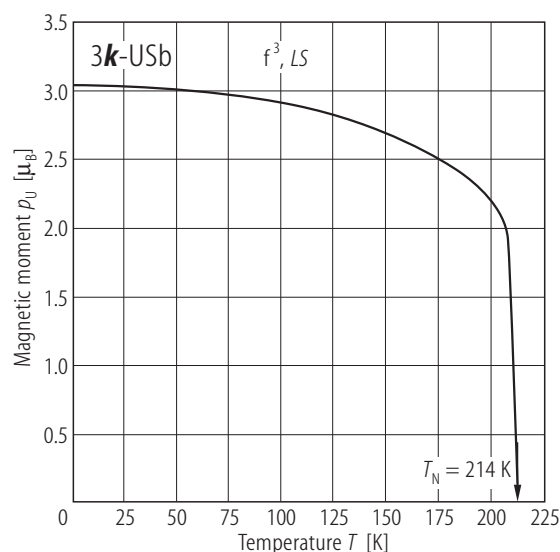


Fig. V.35. USb. Theoretical variation of the ordered moment p_U for the triple- k type I antiferromagnetic structure as a function of temperature [85TC]. Calculations are based on the Hamiltonian assumed from the so-called *hybridization mediated two-ion interaction model* (see[85CSYT]). The phenomenological parameters used in the calculations are: $E_1 = 1$, $H_1 = -0.12$, $W = 0.005$ and $x = 1$. For comparison see similar calculations for UP and UAs presented in Fig. III.26a and Fig. IV.26 (for meaning of the parameters see the Introduction, or the original paper). $p_U^{\text{th}} = 3.05 \mu_B$ ($p_U^{\text{exp}} = 2.82 \mu_B$).

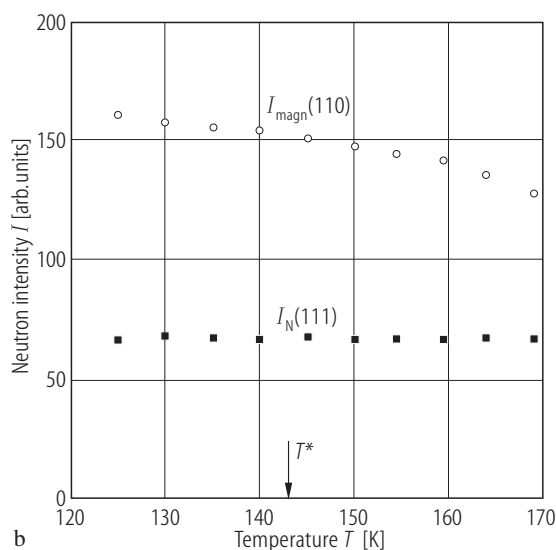
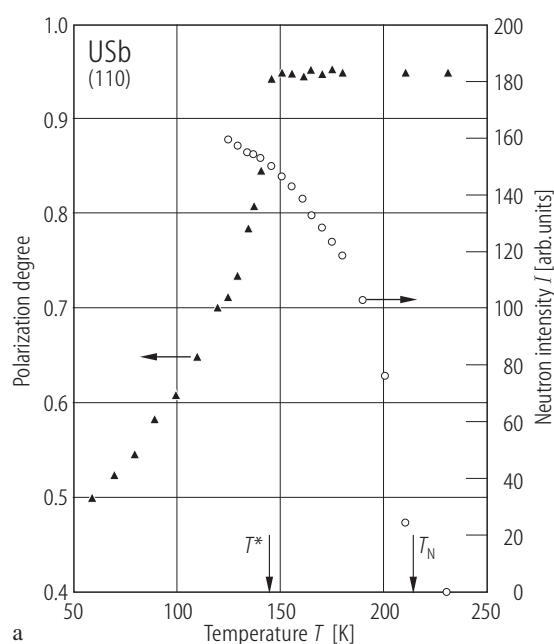


Fig. V.36. USb s.c. Effect of depolarization of polarized neutrons as a function of temperature T . **(a)** Variation of the polarization P (solid triangles) (lhs) and intensity of the magnetic peak (110) (open circles) (rhs), both as a function of temperature [95LS]. The change in P starts below $T^* \approx 143$ K. The possible reason is the existing of dynamic microscopic regions to have a ferromagnetic component, caused by variation in the phase angles Φ_i between certain

triple- k components. **(b)** Intensity, I_{mag} , of AF (110) (open circles) and I_N of the nuclear, (111) (solid squares) peaks around T^* [95LS]. Note that no change in these intensities occurs at T^* , which means that neutrons observe a null effect. At the same time at temperatures close to T^* the sudden increase in the relaxation rate of muon spectra (Fig. V.78) and the sudden dumping of the spin-wave excitations (Fig. V.39) take place.

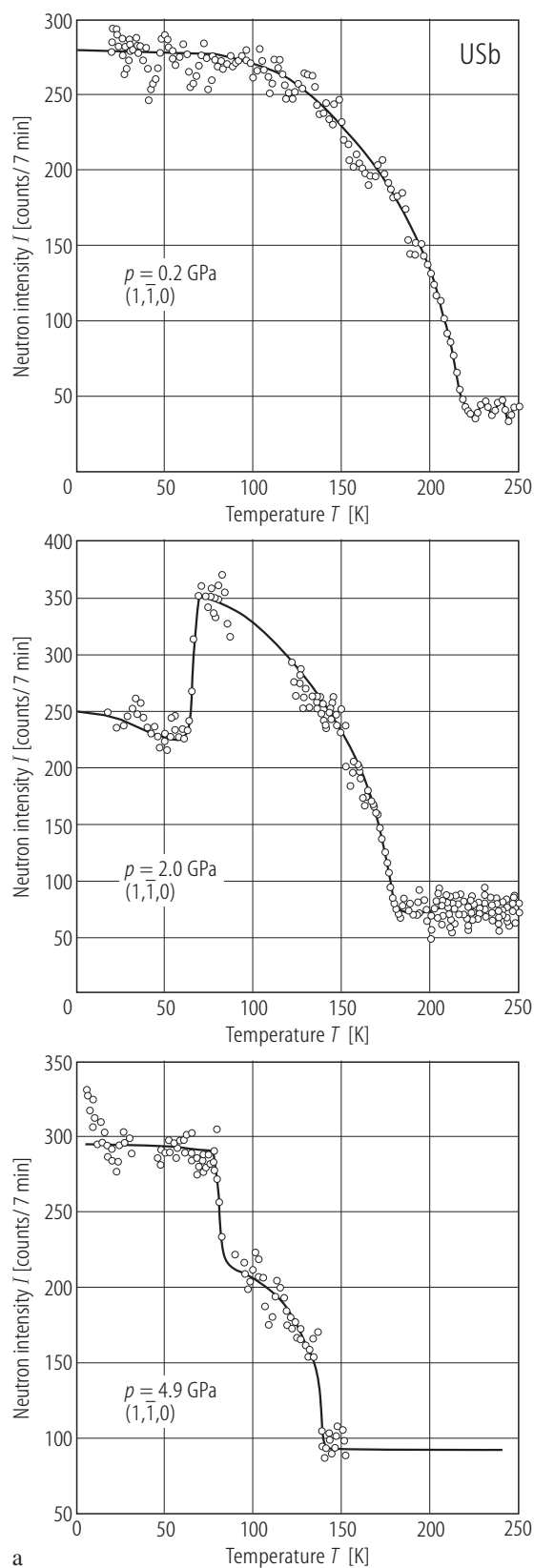
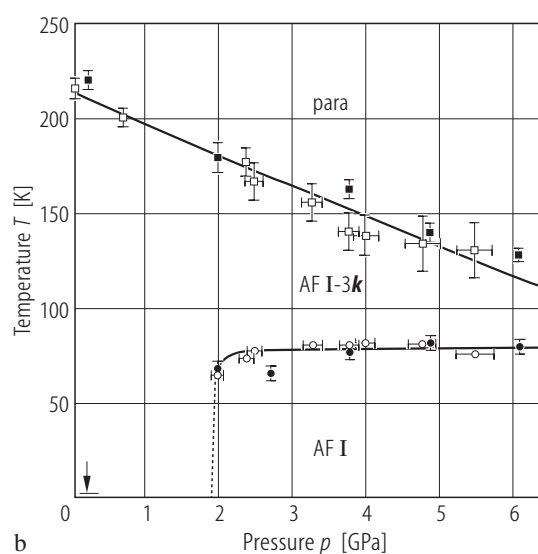


Fig. V.37. USb s.c. **(a)** The neutron diffraction intensity, I , of the $(1, \bar{1}, 0)$ magnetic reflection measured under three different pressures: 0.2, 2.0 and 4.9 GPa as a function of temperature, T , [96MGBV]. Note that the uniaxial stresses affect the balance of magnetic domain population of the triple- k phase at pressures $p \geq 2.0$ GPa giving rise to the formation of single- k -phase at low temperatures. **(b)**. Magnetic phase diagram under pressure up to 6 GPa [96MGBV].



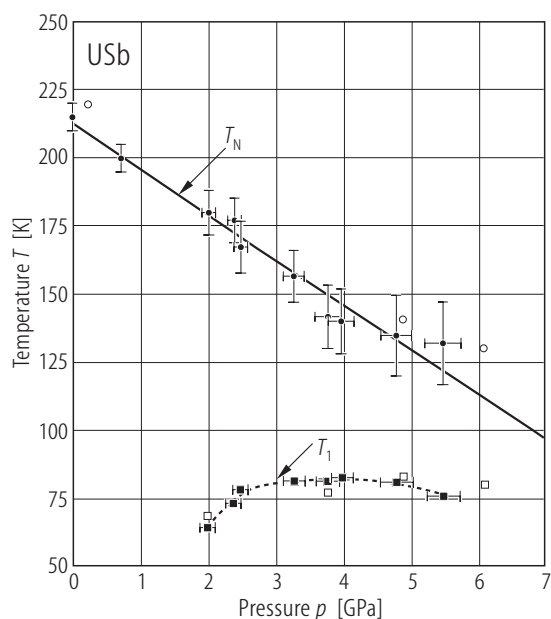


Fig. V.38. USb s.c. Magnetic phase diagram (T , p MPD) under pressure up to 6 GPa derived on the basis of neutron (open squares and open circles) [96MGBV] and of the resistivity results (closed squares and closed circles) [96BGM0].

For Fig. V.39 see next page

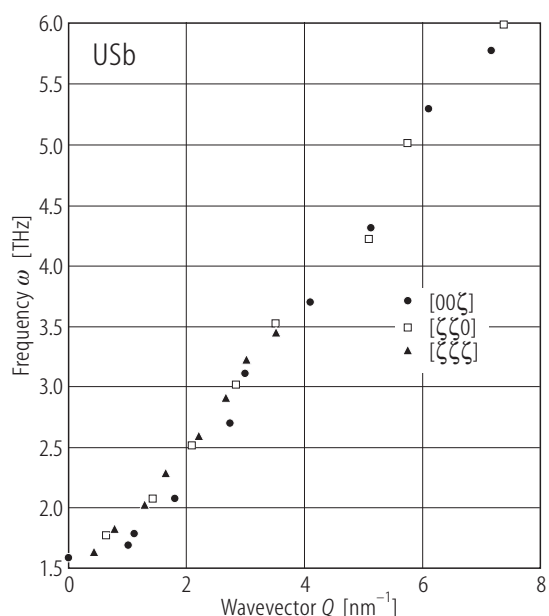


Fig. V.40. USb s.c. Spin-wave frequencies, ω , for the $[00\zeta]$ and $[\zeta\zeta0]$ directions [80LS] and $[\zeta\zeta\zeta]$ direction [88HSL] as a function of scattering wave vector Q . Note the isotropic spin-wave dispersion relation. At a frequency of 6 THz it merges with a band of weak magnetic scattering observed throughout the BZ.

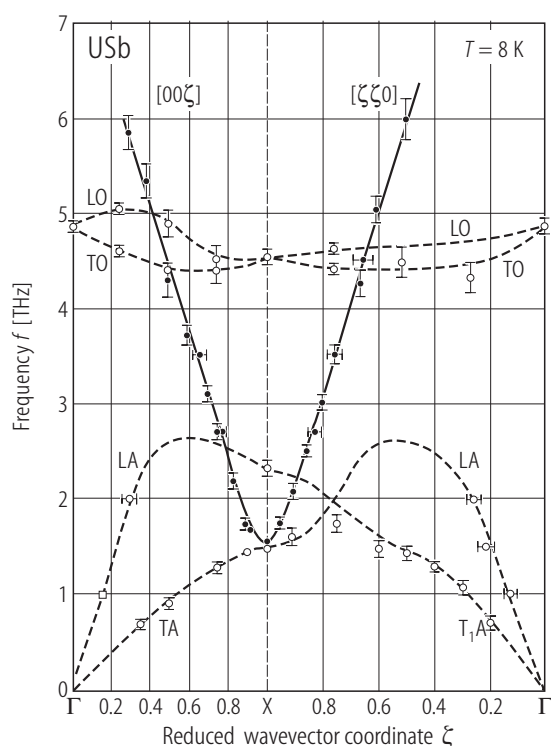


Fig. V.41. USb s.c. The frequency, f , as a function of wave-transfer Q ($\zeta = Qa/2\pi$). Magnetic collective excitations below 6 THz (solid line) together with the phonon dispersion curves (dashed lines) and measured points (closed and open circles, respectively) at 8 K [79LSV1, 2]. Note that the spin-wave excitation is degenerate with the zone-boundary, transverse acoustic phonons at $Q = [110]$ (X points) with a frequency of 1.53(5) THz (≈ 74 K). This is considered as accidental and there is no strong magnetoelastic coupling in USb. (See also LB III/12c, p.431, Fig.50).

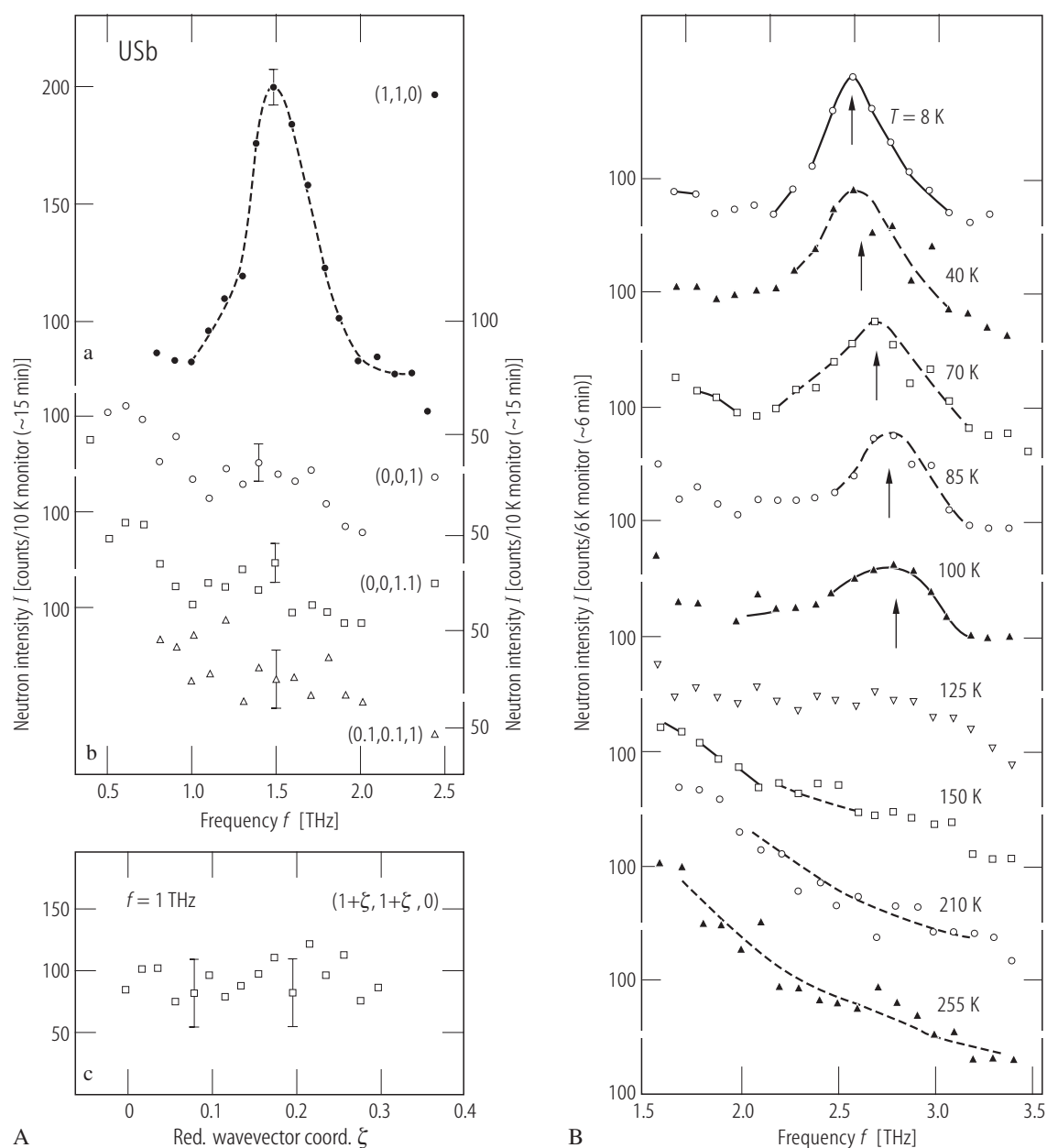


Fig. V.39. USb s.c. **(A)** The magnetic excitations (constant- Q scan) taken at 8 K at the X point seen at **(a)** (110) but not seen at **(b)** (001) or near this point, which is signature of the triple- k structure. Such an observation makes the excitations entirely longitudinal in nature. **(c)** The scan at 1 THz through the (110) position. This confirms the lack of the lower

branch of the magnetic excitation. **(B)** The magnetic excitation intensity, I , at the point (1.15, 1.15, 0) at various temperatures between 8 and 255 K ($T_N = 241.2$ K). Note that the magnetic excitations are essentially unobservable above 125 K, i.e. above $\sim T_N/2$ [79LSV1, 2].

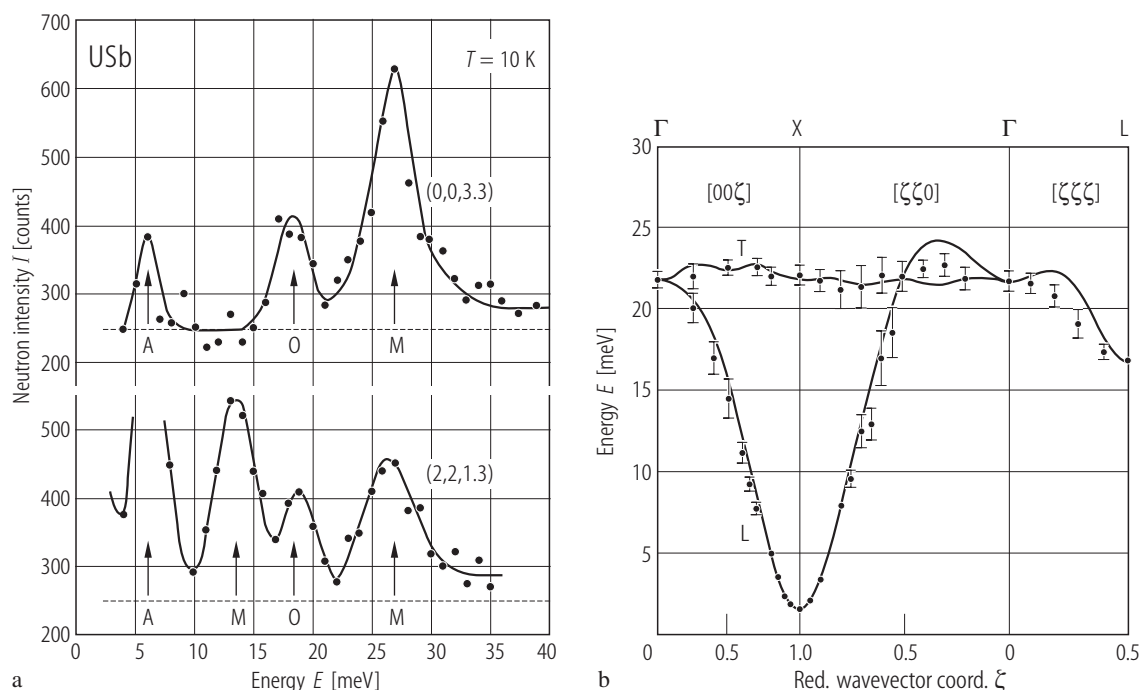


Fig. V.42. USb s.c. **(a)** Constant- Q scans near (003) and (221) positions [85HV], [86HF]. The arrows point to positions of the magnetic excitation (M), the acoustic (A) and optical (O) phonons taken for $E_Q = 14.9$ meV. Note two sharp excitations at about 13 and 26 meV, which can be understood as forms of transverse spin waves in AF-I structures (see Fig. R.16 and work [81JB]). **(b)** Magnetic excitation spectrum [85HV], [86HF], which is consistent with the first measurements of the lower excitation branch reported by [79LSV1, 2]. L and T denote the longitudinal mode (with the anisotropy gap of ~ 6.4 meV at the X points)

and the almost dispersionless transverse mode of 25 meV, respectively (see [81JB]). The solid lines are based on an RPA treatment of a Hamiltonian with a crystal field part and anisotropic bilinear exchange interactions: $H = B_4(O_4^0 + 5O_4^4) + B_6(O_6 - 21O_6^4) - \sum_{aij} J^{aa}(R_{ij})S_i^a S_j^a$, where the LLW parameters are: $x = 0.82(1)$ and $W = 1.9(2)$ meV and $J^{aa} = 1.48(5)$ meV. The crystal electric field favours the $3k$ -spin alignment with $p_U^{\text{calc}} = 2.73(5) \mu_B$ and $T_N = 240(30)$ K and the ratio of the inverse correlation lengths $\kappa_{\parallel}/\kappa_{\perp} = 5(2)$, all these are close to the experimental parameters.

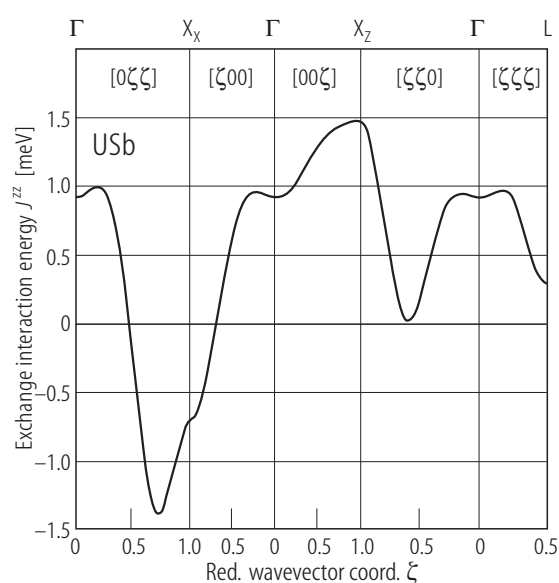


Fig. V.43. USb. The resulting zz component of the Fourier-transformed exchange interaction tensor $J^{zz}(q)$ along the different symmetry directions based on RPA calculations [86HF].

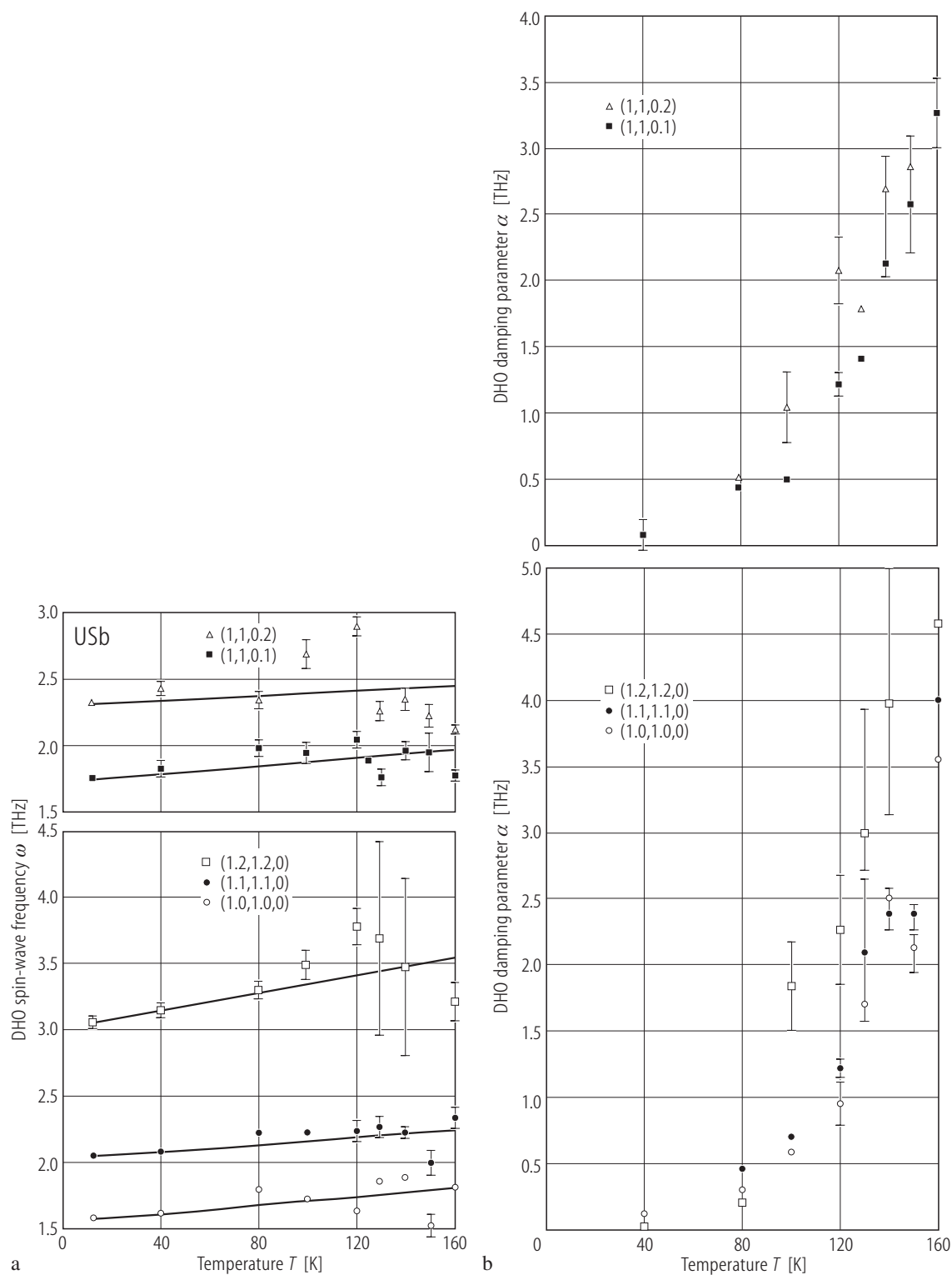


Fig. V.44. For caption see next page

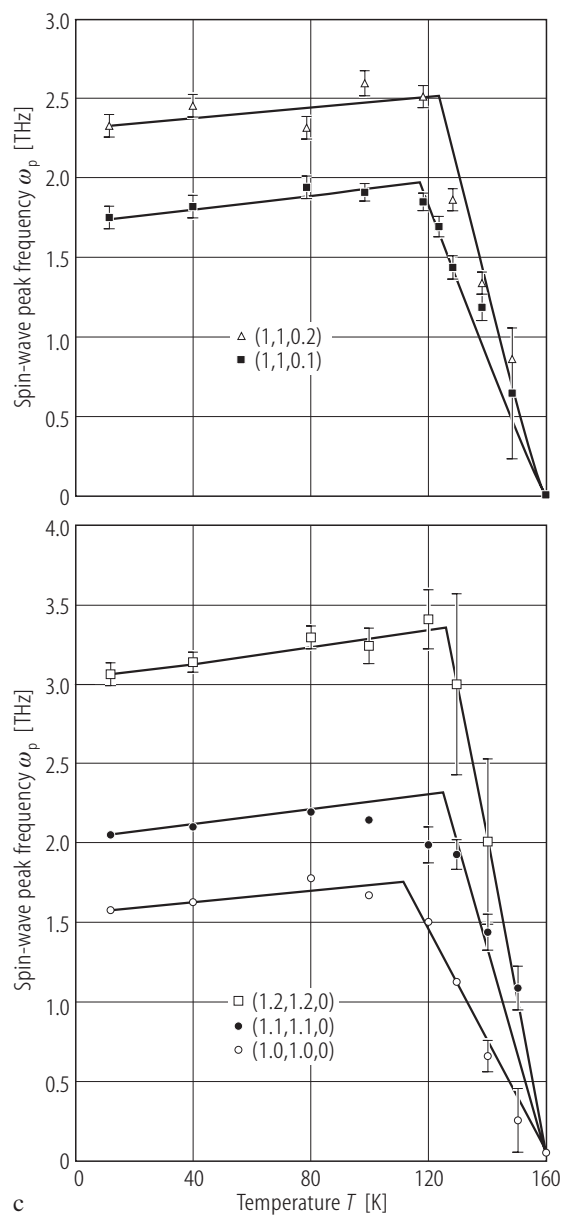


Fig. V.44. USb s.c. INS: Spin waves for five wave vectors, Q , close to the (110) AF Bragg position at various temperatures from 12 to 160 K [88HSL]. Temperature dependences of principal fitting parameters obtained from the DHO (damped harmonic oscillator) – line shapes. **(a)** Intrinsic spin-wave frequency $\omega(q)$, **(b)** spin-wave damping $\alpha(q)$ and **(c)** the scattering peaks $\omega_p(q)$. The solid lines are guides to the eye. The characteristic frequency of the Lorentzian $\Gamma(q)$ is approximated by relation: $\Gamma(q) = \omega^2(q)/\alpha(q)$. Note from **(b)** and **(c)** that spin waves in the temperature range from 100 to 160 K are progressively damped and above $T = 0.75T_N$ ($T_N = 212.30(5)$ K) they are collapsed into broad inelastic scattering that peaks only at zero-frequency **(c)** which is characteristic of magnetic critical scattering.

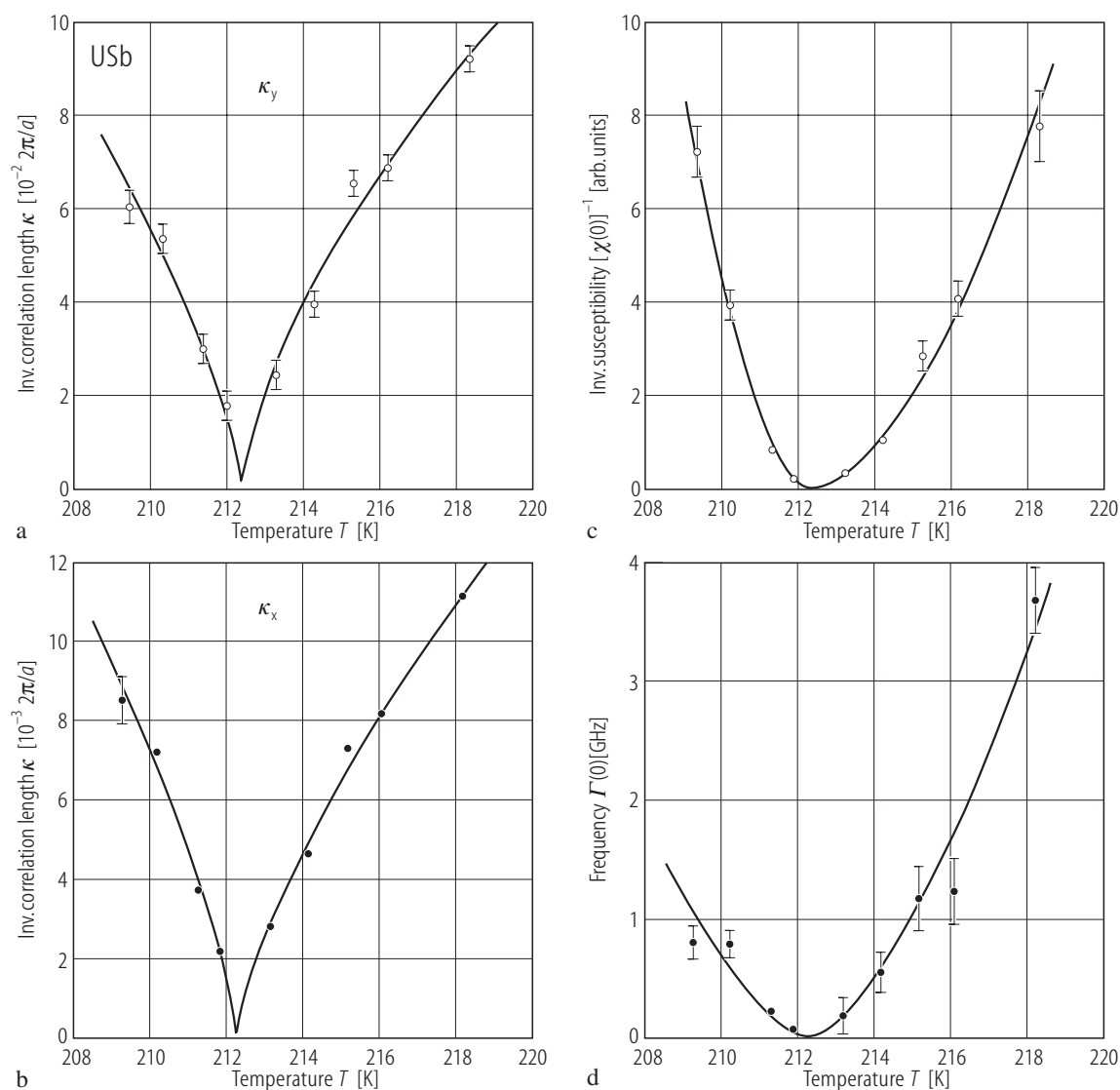


Fig. V.45. USb s.c. INS: Inverse correlation lengths (a) κ_y and (b) κ_x as well as the inverse static susceptibility (c) $[\chi(0)]^{-1}$ and the characteristic frequency (d) $\Gamma(0)$ as a function of temperature studied by neutron scattering

[88HSL]. The solid lines are the power-law fits. The symbols are defined by spectral weight function $\Gamma(q, \omega)$ of a Lorentzian form and by indexes γ , ν , Δ and T , respectively (see also the text). $T_N = 212.30(5)$ K.

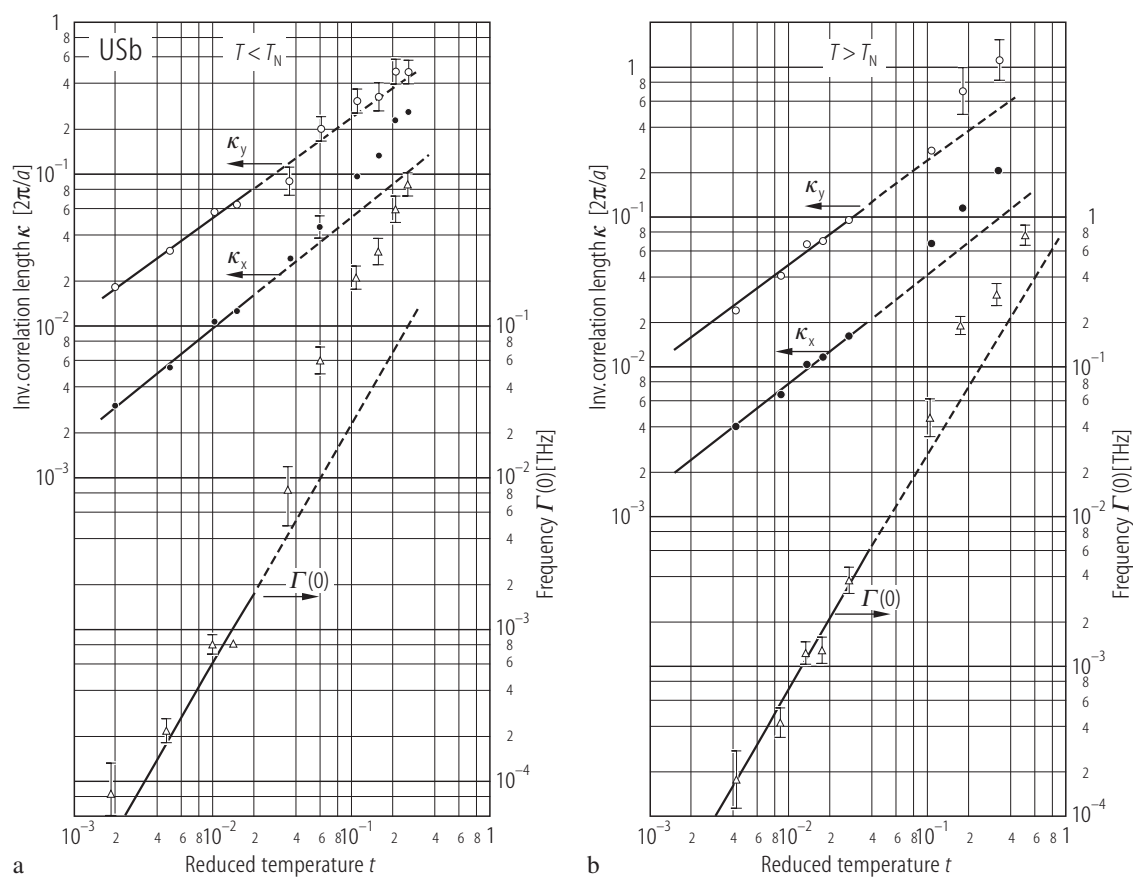


Fig. V.46. USb s.c. INS: A log-log plot of inverse correlation lengths κ_x and κ_y and the characteristic frequency $\Gamma(0)$ examined by neutron scattering as a function of reduced temp. t ($= (T - T_N)/T_N$) for the temperature ranges **(a)** $T < T_N$ (220...160 K) and **(b)** $T > T_N$ (212...320 K) [88HSL]. The solid lines are the power-law fits within the

critical region, which are extended by dashed lines. $T_N = 212.30(5)$ K. The critical amplitudes assumed to be the same above (+) and below (−) T_N :

$$\begin{aligned} \chi(0, T) &= \chi^\pm |t|^{-\gamma}, & \kappa_x(T) &= \kappa_x^\pm |t|^{\nu_x}, \\ \kappa_y(T) &= \kappa_y^\pm |t|^{\nu_y}, & \Gamma(0, T) &= \Gamma^\pm(0) |t|^\Delta. \end{aligned}$$

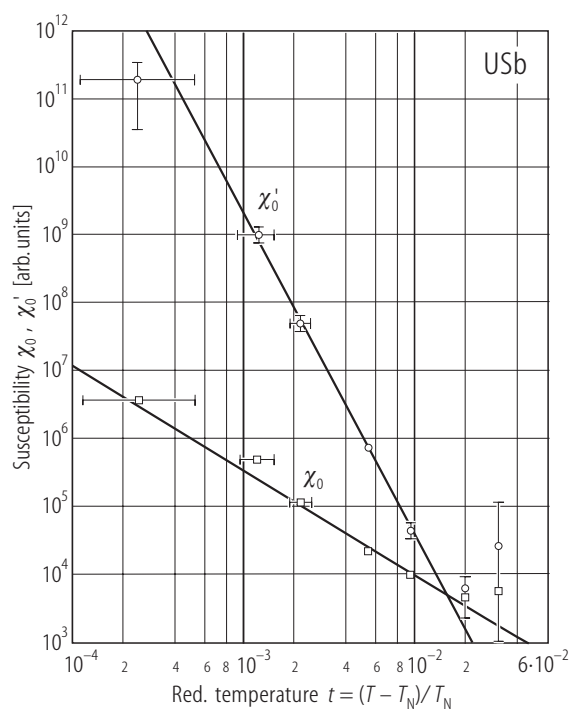


Fig. V.47. USb s.c. RXMS: Static susceptibility of broad (χ_0) and narrow (χ_0') two components vs. reduced temperature, t , in the log-log plots for the (003) critical scattering position [96PNSL]. For explanation of two critical scattering components see Fig. V.56. The solid lines are fits to the power law: $\chi_0 = At^{-\gamma}$ or $\chi_0' = Bt^{-\gamma'}$, $\gamma = 1.54 \pm 0.14$ and $\gamma' = 4.8 \pm 1.3$. The high values for the narrow component excludes the 3D Heisenberg value ($\gamma = 1.4$).

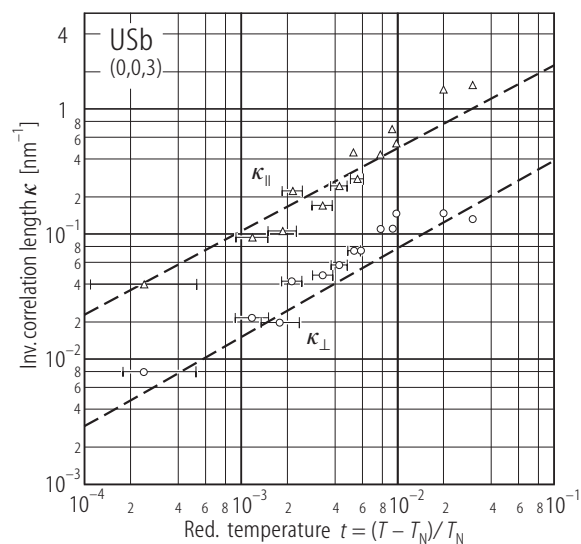


Fig. V.48. USb s.c. RXMS: Inverse correlation lengths, $\kappa_{||}$ (triangles) and κ_{\perp} ($T > T_N$) (circles), of the broad component as a function of reduced temperature, t , at the (003) position probed by X-ray scattering experiment [96PNSL]. Note good agreement to the power-law fits $\kappa_i \sim t^{-\gamma_i}$ (i denotes parallel or perpendicular components) of neutron data (dashed lines) [88HSL]. The temperature dependence of the broad Lorentzian component indicates critical properties consistent with 3D-Heisenberg behaviour.

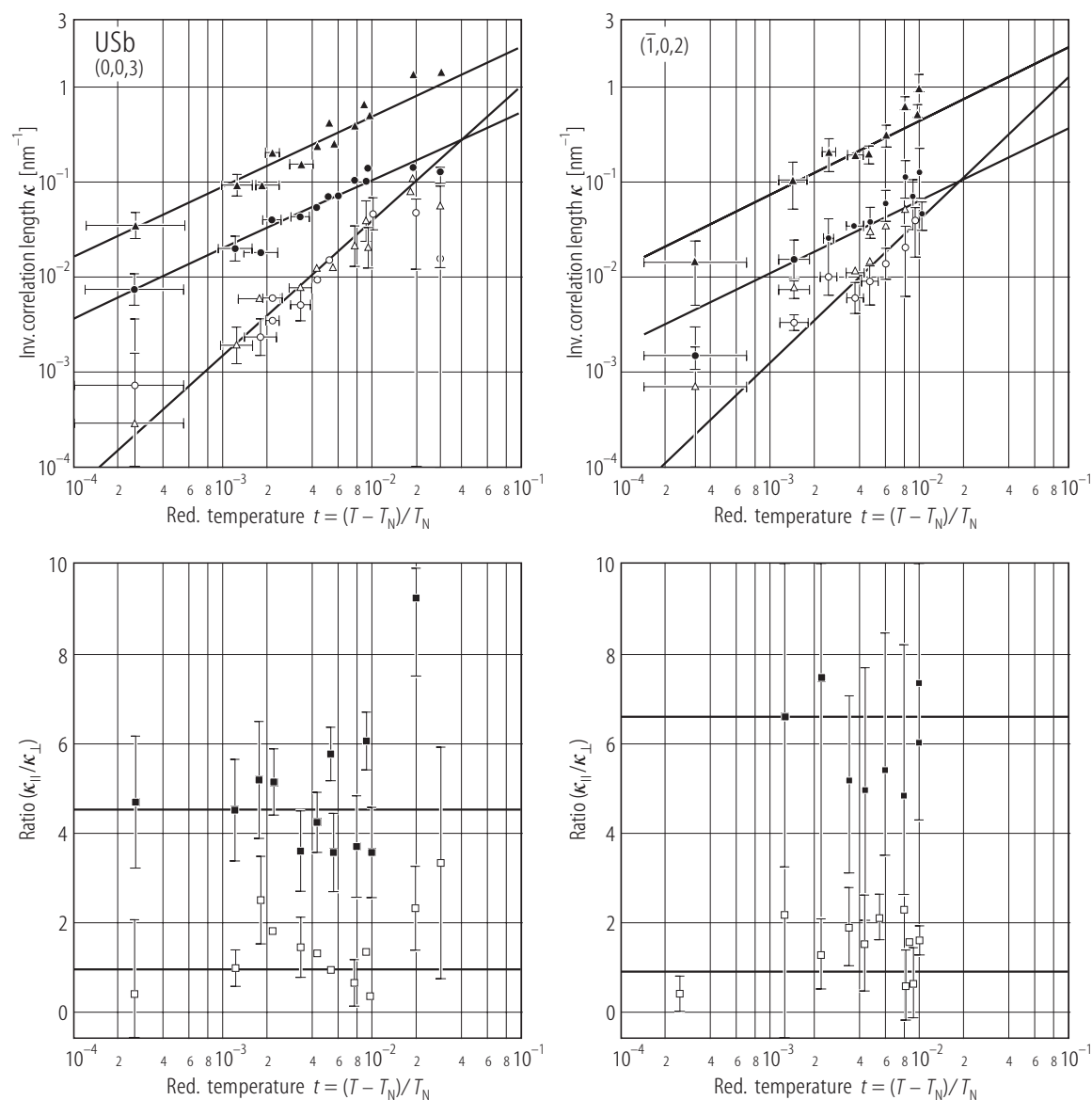


Fig. V.49. USb s.c. The critical scattering above T_N at the (003) and $(\bar{1}02)$ positions measured by X-ray resonance scattering technique (XRES). Upper panels: inverse correlation lengths κ_i as a function of reduced temperature t for (003) (lhs) and $(\bar{1}02)$ (rhs) positions [96PNSL]. Measurements were in the directions parallel (triangles) and perpendicular (circles) to the propagation direction. The

open and closed symbols represent values for the narrow and broad components, respectively. The solid lines through the former symbols give $\nu' = 1.3$ while for the latter symbols $\nu = 0.71$ (3D Heisenberg value). Lower panels (labeled as squares): the anisotropy ratio $(\kappa_{||}/\kappa_{\perp})$ of the data points shown in upper panels. The results for the broad component are in agreement with neutron data [88HSL].

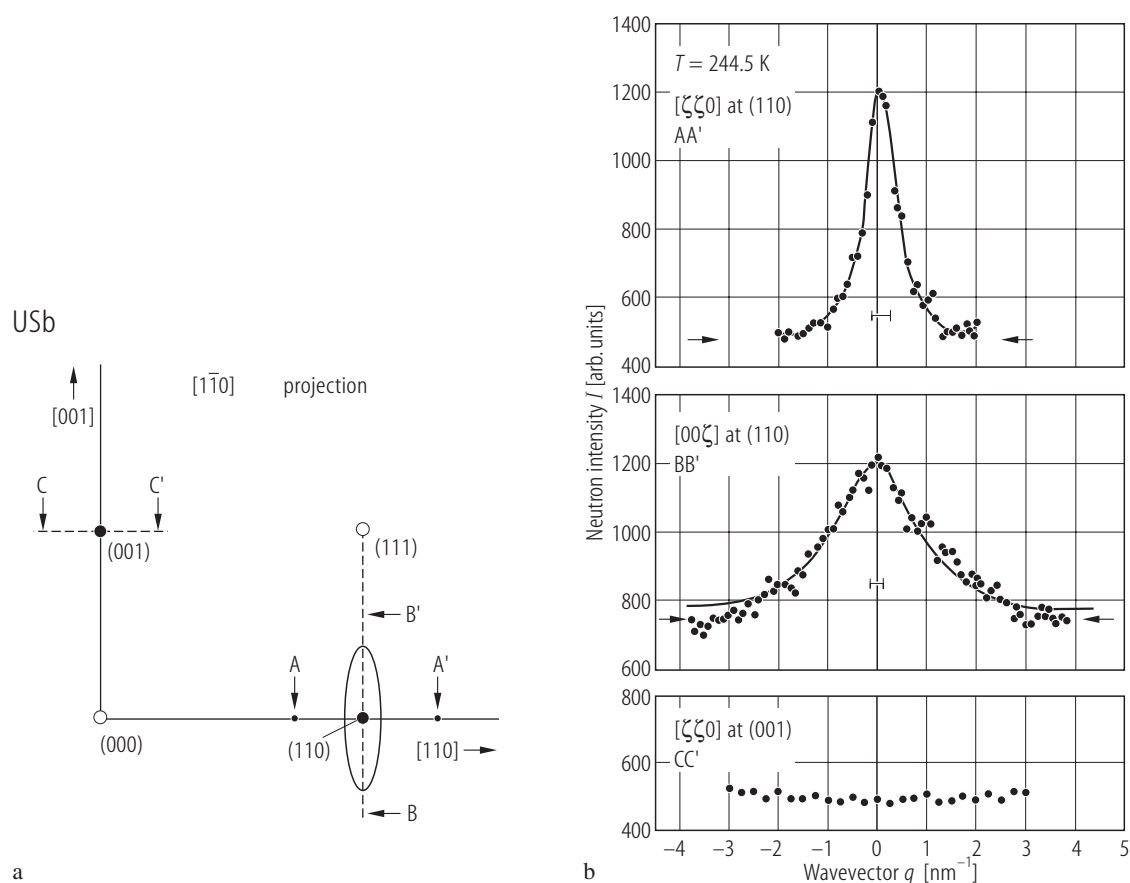


Fig. V.50. USb s.c. Neutron diffraction study. **(a)** The $[1\bar{1}0]$ projection of the reciprocal lattice [78LSSV]. The (001) and (110) are magnetic points. Note that no transverse fluctuations of the spin systems are observed around the (001) point or equivalent (100) and (010) points along $(\zeta\zeta 0)$ (CC'), at any temperature. The critical scattering at the (110) positions represents the longitudinal susceptibility

(see $[\zeta\zeta 0]$ (AA') and $[\zeta 00]$ (BB') directions). The contours form rods of intensity being not observed in cubic materials. **(b)** The corresponding scans at $T_N + 3$ K [78LSSV]. See alternative explanation that the critical scattering, either longitudinal or transverse, in any of the three $\kappa = (001)$ domains is unobservable in the (001) position [88HSL]. (See also LB III/12c, p.430, Fig. 49).